FACULTY OF SCIENCE AND TECHNOLOGY

BACHELOR THESIS

Study programme / specialisation:
Kjemi og miljø

The spring semester, 2022

Open

Author:
Jone Heramb Damås

Jone Damås
(signature author)

Supervisor:
Sachin Murati Chavan

Thesis title:
Carbon capture: Characterization of CO_2 adsorption
by Metal-organic frameworks and Zeolite

Credits (ECTS): 30

Keywords:
CCS
MOF
Adsorption
Selectivity

Pages: 42

+ appendix: 11

Stavanger, 21.05.2022
date/year

Carbon capture: Characterization of CO_2 adsorption by Metal-organic frameworks and Zeolite

By

Jone Heramb Damås

Bachelor of Science
University of Stavanger 2022

Abstract

This work aims to synthesize and characterize the Metal-organic frameworks (MOFs): MIP-202, MOF-801, and a cerium-based version of the MIP-202, and evaluate their potential for use in carbon capturing by the use of adsorption. An outsourced Zeolite-13X molecular sieve was also tested alongside the MOF samples, to compare the results. Stability, crystallinity, and composition were concluded with PXRD, TGA, SEM, and EDS measurements, which were determined on all samples and gave expected and satisfactory results. The EDS results of the MIP-202 and MOF-801 samples revealed a substantial chlorine content in the MOFs, which came from the $ZrCl_4$ salt they were synthesized from. An attempt to remove these and other traces of excess linkers was made by making new samples by washing the MOFs with different solutions, including methanol and acetic acid. The washed samples were tested alongside the untreated MOF and Zeolite-13X samples. Only the MOF-801 samples and the Zeolite-13X gave satisfactory sorption results, as the MIP-202 had collapsed after 60°C degassing, and the Ce-MIP-202 did not adsorb considerably to be further analyzed. Based on BET calculations, the best MOF-801 had a specific surface area of 936.5 m^2g^{-1}, with a total pore volume of 0.4683 cm^3g^{-1}. The Zeolite-13X specific surface area was calculated to be 577.7 m^2g^{-1}, with a total pore volume of 0.2963 cm^3g^{-1}. Both these sample classes demonstrated high selectivity between CO_2 and N_2, but where the Zeolite expressed a much steeper CO_2 adsorption isotherm, which could be disadvantageous when desorbing in industry.

Acknowledgments

"Physics is like sex: sure, it may give some practical results, but that's not why we do it."

- Richard P. Feynman

I would like to take this opportunity to thank the University of Stavanger, the department of chemistry, bioscience, and environmental engineering, and my thesis supervisor Associate Professor Sachin Maruti Chavan for guiding me through the bachelor thesis work. I would also like to acknowledge Dagfinn Søndenaa Sleveland, Stian Penev Ramsnes, and Caroline Ruud for the thorough training on the equipment I used during the thesis work. Finally, I would want to thank my family and girlfriend Louise for always being supportive of my work.

Abbreviations

UNFCCC	United Nations Framework Convention on Climate Change
CCS	Carbon Capture and Sequestration/Storage
CCUS	Carbon Capture Utilization and Sequestration/Storage
IUPAC	International Union of Pure and Applied Chemistry
MOF	Metal-organic framework
MIP	Materials of the Institute of Porous materials from Paris
MMM	Mixed Matrix Membrane
PXRD	Powder X-ray Diffraction
TGA	Thermogravimetric analysis
BET	Brunauer-Emmett-Teller theory
PSA	Pressure-swing Adsorption
TSA	Temperature-swing Adsorption
DMF	Dimethyl formamide
DMSO	Dimethyl sulphoxide
CAN	Ceric ammonium nitrate
RPM	Revolutions per minute
SEM	Scanning Electron Microscopy
EDS	Energy-dispersive X-ray Spectroscopy
IAST	Ideal Adsorbed Solution Theory

Table of Contents

1 Introduction

Increasing worldwide energy demands and climate change caused by greenhouse gas emissions are among the biggest technical challenges of the 21st century, and the situation is frequently getting more severe. In 2015, the United Nations Framework Convention on Climate Change (UNFCCC) established the Paris Agreement, an international treaty aimed at limiting the average temperature increase due to global warming to under 2°C by mitigating greenhouse gas emissions of the signed countries. As a part of the agreement, countries are required to implement measures to reduce their emissions, such as carbon taxes and subsidies. (UNFCCC, 2020).

As the tax on releasing CO_2 into the atmosphere increases regularly, the incentive for companies to manage their emissions gets increasingly stronger. This incentive raises the demand for carbon capture and sequestration (CCS) solutions and therefore opens a window for new opportunities to further develop and broaden the range of different carbon capture technologies to perfectly fit their requirements. CCS, a solution that resolves the emission problems at their root locally, could be an important contributor to reducing global CO_2 emissions, while simultaneously avoiding a reduction in the industrial productivity and expansion. Especially industries such as power generation by coal, cement production, metallurgy, and the oil and gas sector have large CO_2 emissions and thus huge potential to save money through CCS solutions to boost overall profits while simultaneously contributing to reducing overall emissions (Chaudhary & Prasad, 2021). The differences in capture conditions and feed compositions open up for a range of challenges, and the technique for capturing CO_2 is therefore difficult to generalize. Capturing CO_2 from a combustion process where the gas stream mostly consists of N_2 would for instance need a different procedure than removing CO_2 for gas sweetening of a natural gas stream, as gas composition and capture conditions such as feed gas temperature, pressure, and gas composition would differ in each case. There is therefore a large repertoire of different capturing solutions that have been created and implemented through the years in the CCS field.

The CCS term has later been expanded to a broader term: Carbon Capture Utilization and Storage (CCUS), now including the utilization of captured CO_2 rather than just permanent storage. Synthetic fuels made from captured CO_2 and hydrogen are one of the potential applications to utilize captured CO_2 while simultaneously producing fuels that could be burned with net-zero emissions, contributing to the goal of reducing total emissions (Patterson et al., 2019).

2 Literature Review

2.1 Carbon capture

Carbon capturing is the first of the three stages in a CCS operation value chain, the proceeding stages being transportation and sequestration. There are mainly three categories of carbon capture, pre-combustion, post-combustion and oxyfuel combustion. Pre-combustion carbon capture refers to the removal of CO_2 from fuels before combustion is commenced, where CO_2 scrubbing of natural gas from a gas field falls under this category. Post-combustion captures the CO_2 from the flue gas after combustion of fuels. Compared to normal combustion which burns in air, Oxyfuel combustion uses nearly pure oxygen gas, which in turn increases the concentration of CO_2 in the flue gas (Stanger et al., 2015). There are numerous different separation techniques when separating CO_2 from flue gas or other gas streams. Chemical absorption by amines, which is the most widespread carbon capturing solution, has since 1996 been capturing CO_2 on the Sleipner oil and gas field on the Norwegian continental shelf and injecting it for permanent storage in saline aquifers below the reservoirs at a rate of 2800 tonnes per day (Hosa et al., 2010). The use of methods such as adsorption or membrane separation has not been as frequently used, but are nowadays being research and tested on a greater scale, as new technologies in this field have emerged. The adsorption method of carbon capture uses a solid compound to bind CO_2 in contrast to the liquid amines used in absorption. The physics and mechanics of the gas binding is quite different between the two as well. Adsorption for example uses Van der Waals forces, in some cases ionic or covalent chemical bonds, to bind the gas molecules to the material, while in the case of absorption, the gas molecules enter a liquid bulk phase by the gas-liquid equilibrium principles of Henry's law. The adsorption process is exothermic and favors low temperatures, while the absorption process is endothermic and is not affected too much by temperatures (Geankoplis, 2003).

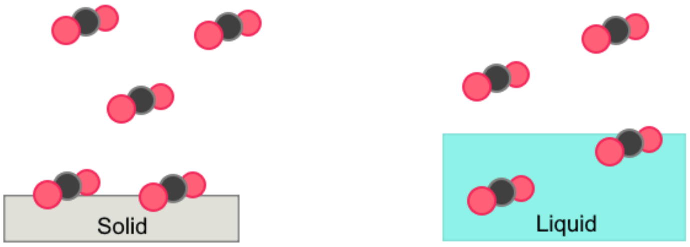

Figure 2.1. Comparison of the mechanics CO_2 adsorption has onto a solid surface (Left) and the absorption of CO_2 molecules into a bulk liquid (Right)

Carbon capture by absorption and adsorption both have their advantages and disadvantages when compared to each other, and have therefore different applications, depending on the operation. The mass transfer between the adsorbent and the adsorbate is approximately three times larger than that between CO_2 and amine, and with a greater contact area between the phases, which makes adsorption a more effective process compared to absorption when desiring to get CO_2 concentrations at a minimum in the output stream. Adsorption processes suffer however from limited loading capacity, and are therefore disadvantageous when treating gas streams with high CO_2 concentrations or when operating at low pressures. There are also other factors that play in such as corrosion from amine in an absorption process, or the uptake of unwanted gases or moisture to the adsorbent when doing adsorption (Yu et al., 2012).

2.2 Adsorption mechanics and isotherms

Adsorption is a phenomenon where chemical species like ions or molecules are adhered to the surface of a solid or sometimes the surface of a liquid. The fluid that gets adsorbed is called the adsorbate and the solid materials which the fluid is adhered to are called the adsorbent. The differences in adsorption affinity for different gases make adsorptive materials functional for gas-gas and gas-liquid separation. The mechanics of adsorption is often divided into two categories: Physical adsorption and chemical adsorption, often shortened to physisorption and chemisorption respectively. Physisorption adheres molecules to the solid by Van der Waals forces, a relatively weak interaction force between molecules, while chemisorption adheres molecules by a greater force by establishing covalent or ionic bonds between the adsorbate and adsorbent. Physisorption is non-specific, meaning it does not differentiate between the different species adsorbed. In terms of physisorption, the pore structure of porous materials has been classified by IUPAC into three categories: Macropores, which contain pores with diameter exceeding 50 nm, mesopores, with diameter between 2 nm and 50 nm, and micropores, where the pore diameter is below 2 nm (Thommes et al., 2015).

Isotherms show the amount of adsorbate that has been adsorbed on the adsorbent as a function of relative or absolute pressure in gas-solid adsorption, and concentration in liquid-solid adsorption. There have been constructed several different mathematical models to fit different types of experimental isotherm data, where the Langmuir and Freundlich isotherms are some classical examples. The Brunauer-Emmett-Teller (BET) theory, which is a more extensive isotherm model, extends on the principles of the Langmuir adsorption model by implementing multilayer adsorption. The BET model is also useful for finding the specific surface are of microporous materials, by transformations of the BET isotherm function (Galarneau et al., 2018).

The gas-solid isotherms have been found and categorized by the International Union of Pure and Applied Chemistry (IUPAC) into a set of isotherm types based on isotherm shape, where the six most common are illustrated in figure 2.2. It’s worth noting that some of these isotherms have different desorption isotherms compared to the adsorption like the type IV and V isotherms. Typically, these isotherms are observed on mesoporous materials, and are caused by capillary condensation, a phenomenon whereby multilayered adsorbed gases in the pores condense to form liquid that is more difficult to desorb (Horikawa et al., 2011).

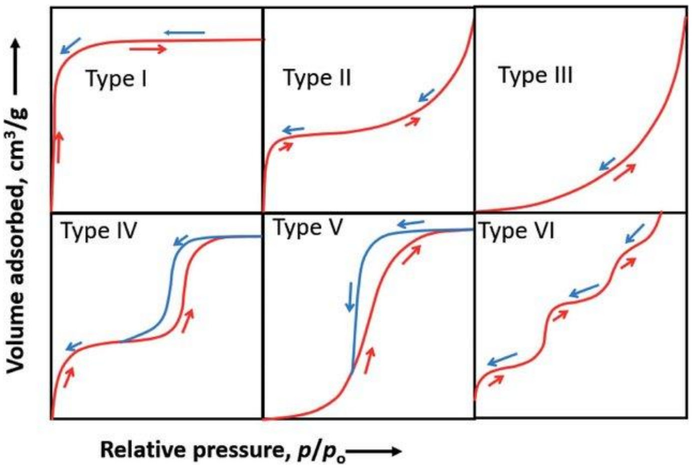

Figure 1.2. Gas-solid adsorption (red) and desorption (blue) physisorption isotherm types, classified by IUPAC, collected from (Kumar et al., 2019)

2.3 Metal-Organic Framework and Zeolite

2.3.1 MOF structure

Metal-organic frameworks (MOFs) are porous hybrid materials consisting of both organic and inorganic components, forming a lattice structure of inorganic metal clusters and organic linkers, which bind the clusters together, usually by the organic linker's carboxylic acid groups, as shown in figure 2.3 below (Farha & Hupp, 2010). The yellow sphere illustrated in the same figure describes the pore in each lattice of the MOF, and is the basis of the many characteristics they possess. The discovery and research of MOFs began in the mid-1990s, which makes the field rather novel. Despite this, a number of different promising applications have already been discovered for MOFs, ranging from gas separation to catalysis to drug delivery to water treatment (Diab, Salama, Hassan, Abd El-moneim, et al., 2021). In light of the current global challenges, including climate change, emerging diseases, and water pollution, these MOF research fields are therefore particularly relevant and interesting.

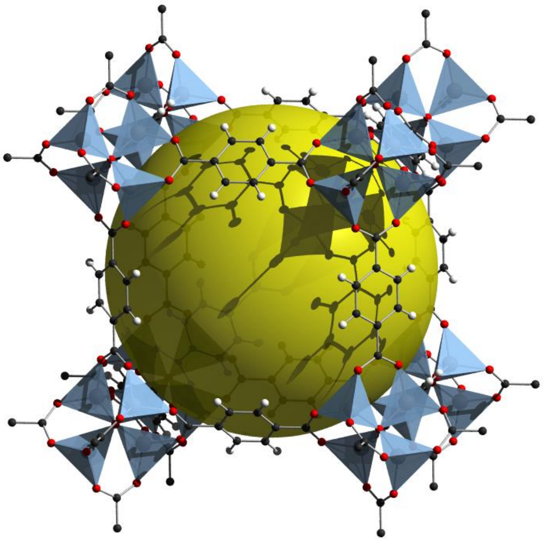

Figure 2.3. MOF-5 unit-lattice structure, where the MOF's lattice pore volume is represented by a yellow sphere. Collected from (Boehle, 2010).

Due to the MOFs pore structure, the internal surface area of the materials is particularly large, thus making MOFs suitable for adsorption applications. There have been reported MOFs with specific surface areas of up to 7839 m^2g^{-1}, which is comparable to the area of a football pitch per gram of material (Hönicke et al., 2018). Due to the MOF's large specific surface area, high gas uptake capacity, and variable and tunable pore structures and properties, the MOFs have presented themselves as a prominent adsorbent for use in carbon capture operations (Yu et al., 2012).

2.3.2 MIP-202 and MOF-801

The MIP-202 (Materials of the Institute of Porous Materials from Paris) a metal-organic framework composed of zirconium clusters and aspartic acid linkers, has been shown to have a significant CO_2/N_2 separation potential. A MOF with similar molecular structure, MOF-801, consists of the same zirconium cluster, only it has fumarate linkers instead of aspartate. It has been reported that MOFs consisting of metal ions like Zr^{4+}, Ti^{4+}, Cr^{3+}, and Fe^{3+} all make stable MOFs when bound with organic linkers with carboxylate groups, and is one of the reasons both MIP-202 and MOF-801 using Zr^{4+} have been shown to be stable under carbon capture conditions (Saidi et al., 2021). The 4-lattice MOF structure of both MIP-202 and MOF-801 is presented below by figure 2.4, where the similarities between them in structure geometry is quite apparent.

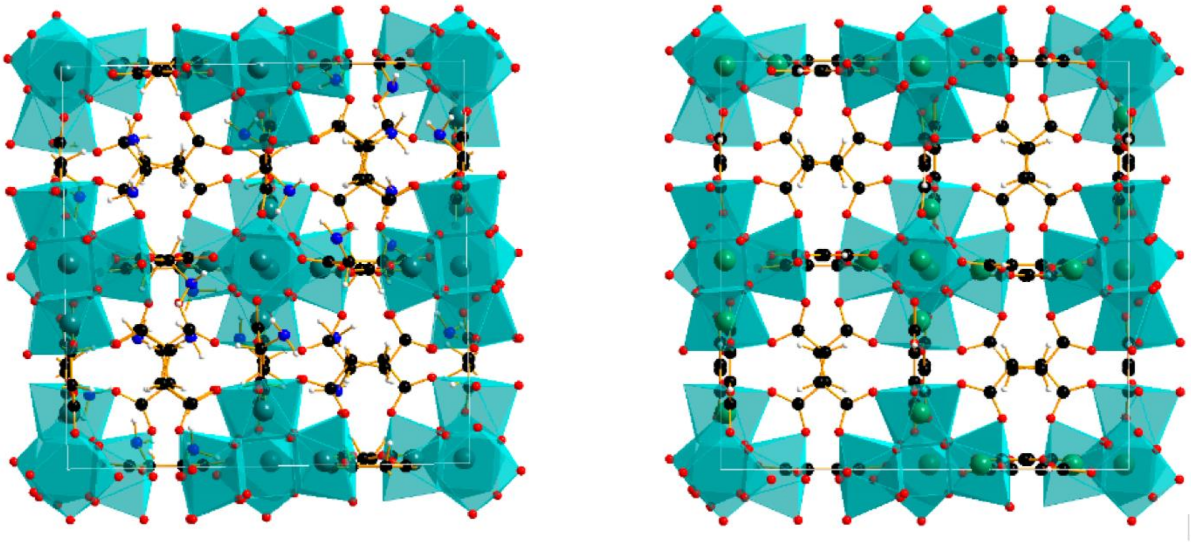

Figure 2.4. Structure of MIP-202 (Left) and MOF-801 (Right), where the zirconium clusters are illustrated in teal boxes, oxygen atoms in red dots, nitrogen in blue, and carbon in black, collected from (Saidi et al., 2021).

The fumarate molecule seen to the right in figure 2.5, does not contain an amine group compared to aspartate, giving the molecule and the created MOF significantly different characteristics and properties, one being that the fumaric acid used in the synthesis of MOF-801 does not have any stereoisomers. The molecules below share however the same placement of the cluster-binding carboxylic acid groups of the linkers and the distance between them, thus explaining the structure similarities.

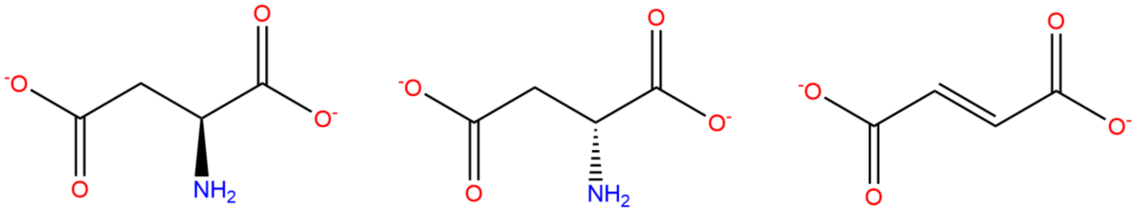

Figure 2.5: (**Left**) L-Aspartate, (**Middle**) D-Aspartate, and (**Right**) Fumarate skeletal structures.

It has been reported that the MIP-202 has a higher affinity for CO_2 than the MOF-801. This is most likely caused by the amine group on the aspartate linker (Saidi et al., 2021). Functional groups like the amine group (-NH_2) in MIP-202 can alter the properties of the MOFs, where the amine groups have a high affinity for acidic gas molecules like CO_2, NO_2 or H_2S, all of which are frequently removed through gas separation in industry. MOFs with amine groups could either be synthesized with amine containing linkers directly, like the MIP-202, or to be attached later through post-synthesis modification (Lin et al., 2016).

2.3.3 Zeolite 13X

As opposed to metal-organic frameworks, Zeolites are completely inorganic, consisting of aluminosilicate crystals of earth alkaline elements. They possess however many of the same properties, like the microporous structure and could therefore be used for gas separation through sorption. They have been used extensively in gas separation fields such as oxygen production from the air (Shokroo et al., 2017). In comparison to the MIP-202 and MOF-801, most zeolites with carbon capturing properties have a range of disadvantages, including expensive materials and the complexity of their synthesis and post-synthesis treatments, contributing to the high cost of their production (Saidi et al., 2021). Its decomposition temperature is much higher (well above 1000°C), compared to MOFs, giving it a considerable advantage in terms of stability in harsh operating environments (Masika & Mokaya, 2013).

2.3.4 MOF synthesis

There is a wide range of different methods for synthesizing MOFs, however, the solvothermal method is the most common. The solvothermal synthesis method is a relatively simple procedure with few steps, but varies greatly in synthesis duration. During the solvothermal process, the MOF substrates are added to a solvent which is heated above room temperature, hence the name of the reaction type. The choice and quantity of solvent is important, as the solvent itself plays a major role in the MOF's synthesis mechanism, as they function as structure-directing agents, aiding the formation of the MOF crystal. An ideal solvent for solvothermal synthesis should be polar and have a relatively high boiling point. Some typical examples of solvents used include water, dimethyl formamide (DMF), dimethyl sulphoxide (DMSO), and alcohols (Soni et al., 2018).

Some synthesis procedures, including the MOF-801 synthesis, require a modulator to aid the formation of the MOF crystal during synthesis, as shown in figure 2.6. The modulator works by binding to the metal cluster by the carboxylic acid group forming an intermediate complex, then exchanges itself with the desired linker in a replacement reaction. The modulator therefore acts as a competitive binder to the metal clusters and would therefore in larger concentrations slow down the replacement reaction, decelerating the crystallization of the MOF, which in turn produces larger crystals (Jahan et al., 2022). Some typical modulators used in MOF synthesis are simple carboxylic acids such as formic or acetic acid.

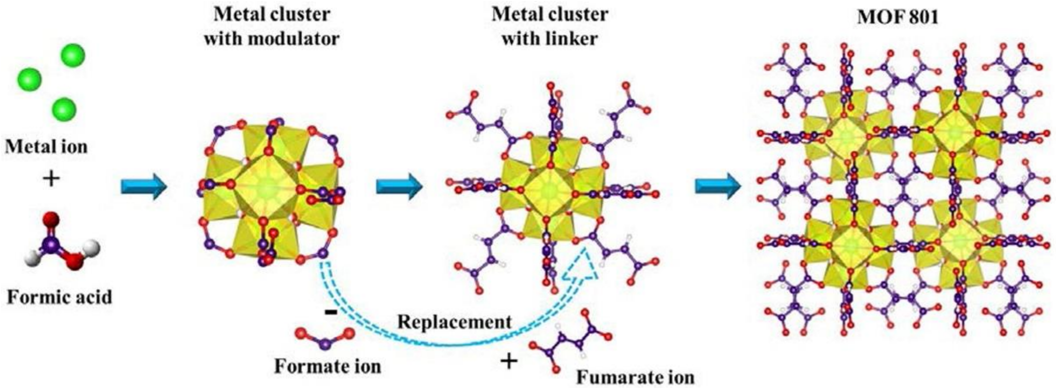

Figure 2.6. Reaction mechanism of a MOF-801 synthesis with formic acid as modulator, collected from (Jahan et al., 2022).

Synthesized MOFs could further be modified in a procedure called Post-Synthesis Modification (PSM) to change the structure and physical properties of the MOF such as increased selectivity for various gas molecules. The zirconium based UiO-66-NH_2 for instance has shown high potential for different post-synthesis modifications, by attaching different functional groups to the amine site of the linker. Amine groups on MOFs have been shown to be both excellent for increasing CO_2 adsorption capacity and to attach other organic units, for example by an imine condensation reaction between the amine on the MOF and an aldehyde (Guo et al., 2021).

2.3.5 Industrial-scale operation

On an industrial scale, CO2 adsorption and desorption would be primarily accomplished through pressure-swing adsorption (PSA) or temperature-swing adsorption (TSA). In a PSA process, the adsorbed gas is desorbed by lowering the pressure, whereas the gas is desorbed by increasing the temperature in a TSA process. Both processes could be illustrated as seen in figure 2.7. Here, the effects on the adsorptivity by the change in pressure could be described as moving along the isotherm. When the temperature is changed, the effect could be described by a lowering of the whole isotherm, decreasing adsorbed amount at all pressures. The shape of the isotherms, selectivity and heat of adsorption are therefore some of the most crucial characteristics when assessing whether the PSA or TSA would be the most effective and energy efficient mode of operation (Broom, 2018).

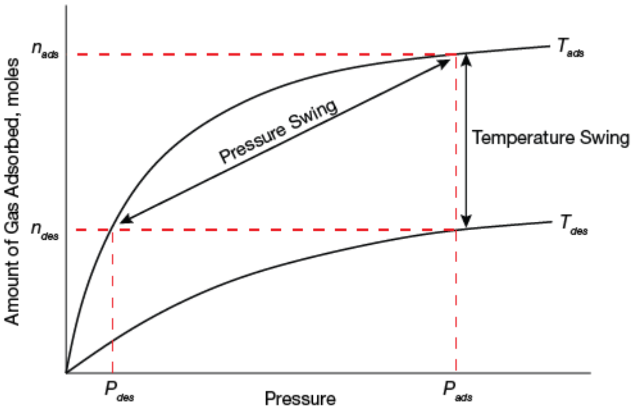

Figure 2.7. Pressure- and temperature-swing effect on the adsorption isotherm, collected from (Broom, 2018).

As the MOFs cannot be used as-is in powder form for a full-scale carbon capture process, they must be pressed into pellets by using a press with specific pressures and durations. The pellets are then placed in a fixed bed adsorption column, where gas will be sent through for gas separation. It has been concluded in (Majchrzak-Kucęba & Ściubidło, 2019) that the MOFs tested in this paper can be effectively pelletized without losing their sorption properties. Metal-organic frameworks like the MOF-801 and UiO-66 could also be applied to membranes for CO_2/N_2 membrane separation. The membranes could for instance be constructed by MOFs together with gas permeable polymers into something called a Mixed Matrix Membrane (MMM). These membranes has shown a promising potential for carbon capture applications (Chen et al., 2020).

3 Thesis objective

The main objective of this thesis is to evaluate different MOFs' potentiality to be used as adsorbents to capture CO_2 by gas separation through characterization and gas uptake measurements, using both CO_2 and N_2 as adsorbates. The MOFs chosen for the analysis are the zirconium and aspartate-based MIP-202, the zirconium and fumarate-based MOF-801. A cerium-based version of the MIP-202 (named Ce-MIP-202 in this thesis) with aspartate linkers were also chosen. To compare the absorption capabilities and material characteristics of the MOFs, an outsourced Zeolite-13X sample was going to be analyzed with the same methods. This thesis also has the objective to undertake some of the future work noted in (Skjærseth, 2021), such as IAST selectivity calculations and isosteric heat of adsorption plots.

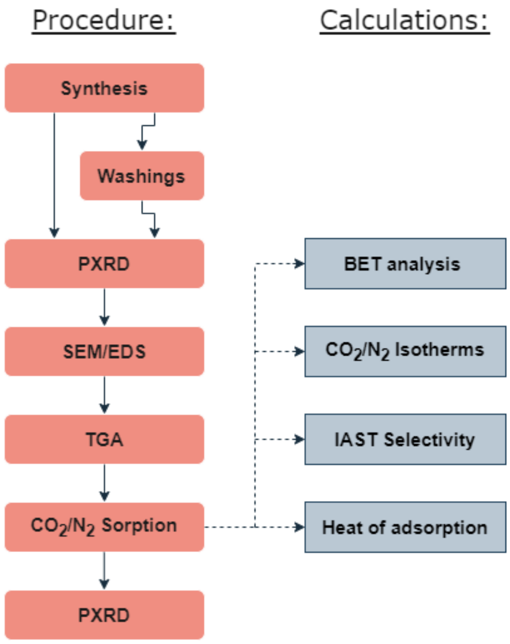

Figure 3. Workflow process diagram.

The experimental procedure is as explained by the flow chart in figure 3, where the MOF samples are first synthesized, and where new samples are created by washings of the synthesized samples. The samples are then taken through Powder X-ray diffraction (PXRD), Scanning electron microscope (SEM), Energy-dispersive X-ray Spectroscopy (EDS), and Thermogravimetric analysis (TGA) to characterize crystal structure, compositions, and stability, before the gas sorption analysis. The Sorption analysis includes N2 sorption at 77K for BET surface area and porosity calculations, and CO2/N2 adsorption analysis at 273K and 293K to create isotherm data for coadsorption, selectivity and heat of adsorption calculations. PXRD is also used after the sorption analysis to check if MOF structure has been damaged. Every sample of MOF synthesized for use in the thesis has been synthesized and treated with an emphasis on substance toxicity and the principles of green chemistry. Therefore, choice of metal ions, linkers, and solvents for synthesis were important factors considering the potential environmental impact of the production procedure and waste disposal when conducted both in the laboratory and in an industrial setting. Low toxicity MOFs also show potential for use in biomedical applications, for instance by using the MOF as a nanocarrier for drug delivery (Sun et al., 2020).

4 Material and methods

4.1 Materials

Zirconium(IV) chloride (≥99.5%, Sigma-Aldrich), DL-Aspartic acid (≥98%, ThermoFischer), Fumaric acid (≥99.0%, Sigma-Aldrich), Ceric ammonium nitrate (≥99%, Fluka chemika), Molecular sieves, 13X (powder, ThermoFischer), Acetic acid (≥99.8% VWR), Formic acid (89-91%, Supelco), Methanol (absolute, VWR), Sodium acetate anhydrous (powder, VWR), Acetone (≥99%, VWR).

4.2 Synthesis and preparation

4.2.1 synthesis of MIP-202, MOF-801, and Ce-based MIP-202

The synthesis method for MIP-202 was obtained from (Diab, Salama, Hassan, El-Moneim, et al., 2021). The MIP-202-01 sample was prepared by the following procedure: 2.3012 g of $ZrCl_4$ was dissolved in 7 ml distilled water in a 50 ml round bottom flask. 2.7486 g of DL-Aspartic acid was then added together with 3 ml of distilled water. The mixture was heated with reflux at 120°C for 24 h with stirring at 400 RPM. The product was filtered and washed with a small amount of distilled water twice, followed by a small amount of acetone. Figure 4.1 illustrates the synthesis setup, which is the same for the proceeding synthetic procedures. The final product collected had a percentage yield of 101.1% and had the appearance of a fine white powder.

The synthesis for MOF-801 was obtained from (Li et al., 2021). The MOF-801-02 sample was prepared by the following procedure: 1.1636 g of $ZrCl_4$ was dissolved by 12.5 ml distilled water, followed by 12.5 ml of glacial acetic acid and 0.5802 g of fumaric acid. The mixture was boiled with reflux at 95°C with stirring at 400 RPM. The product formed after 5 minutes, but was left for 24 h. The product was then centrifuged at 4000 RPM for 15 minutes and then air dried. The final product collected had a percentage yield of 134.26% and had the appearance of a fine white powder.

The synthesis method for the cerium-based MIP-202 was obtained from (Jacobsen et al., 2019). The synthesis method for the cerium-based MIP-202 was obtained from (Jacobsen et al., 2019). The Ce-MIP-04 sample was prepared by the following procedure: 0.954 g of aspartic acid was dissolved in 30 ml of distilled water in a 100 ml round bottom flask. 26 ml of formic acid (89-91%) was added, followed by 9.55 ml of a ceric ammonium nitrate (CAN) solution. The mixture was set up for heating with reflux at 100°C with 400 RPM stirring for 30 minutes. The product was then centrifuged at 4000 RPM for 15 minutes, then washed with 25 ml of acetone before centrifuging again at 4000 RPM. The acetone was then decanted, and the product was set to air dry. The final product collected had a percentage yield of 108.16% and had the appearance of a fine light-yellow powder.

Figure 4.1. Synthesis setup for MIP-202, using a round bottom flask with a stir bar and a reflux condenser on a hot plate.

4.2.2 Solvent washings

A new set of samples were made from all three synthesized MOF types by washing the samples with different solutions. The washings were conducted to try to remove unwanted chemical species in the product, as the samples could contain unreacted linkers and chloride ions in the case of MIP-202 and MOF-801.

A new sample: MIP-202-06 was made of the already synthesized MIP-202-01, by weighing out 1.000 g of the sample and adding it together with 25 ml of methanol to a 50 ml centrifugation tube. The tube was shaken thoroughly and centrifuged at 4000 RPM for 15 minutes. The methanol was then decanted off, and another 25 ml of methanol was added to the tube and centrifuged with the same procedure. After the methanol was decanted off, 25 ml of acetone was added. The tube was shaken, centrifuged at 4000 RPM for 15 minutes, and then decanted. The rest of the centrifuge contents was set to air dry for 24 hours before weighing. The yield of the washing process was 0.8723 grams, with a percentage yield of 87.23%.

A new sample: Ce-MIP-202-07 was made of the already synthesized Ce-MIP-202-04 sample. The same washing procedure as the MIP-202-06 was conducted on 0.2500 g. The finished product was weighed in at 0.2290 g, with a percentage yield of 91.60%. The same procedure was conducted when creating the Ce-MIP-202-08 sample, but with glacial acetic acid as a solvent.

The MOF-801-03 and the MOF-801-09 were both created by weighing out 0.300 g of the already synthesized MOF-801-02 sample and washed with glacial acetic acid and 0.1M sodium acetate solution respectively. Both samples were centrifuged for 15 minutes at 4000 RPM, then washed with acetone before centrifuging again.

4.3 Methods

4.3.1 Powder X-ray diffraction

After the synthesis and post-treatments, powder X-ray diffraction (PXRD) analysis is carried out in order to verify that the right material and structure of the crystalline phases has been achieved. The quality of the crystals and purity of the product is determined by analyzing the PXRD patterns, where sharper peaks with higher counts indicate a pure and well-structured crystal. The pattern is also compared with patterns from literature to verify that the synthesis result is the intended product. The PXRD patterns measured in this thesis were conducted with a D8 Advance Eco from Bruker, scanning with angles between 2° and 70° 2theta. The scanning procedure was conducted with incremental steps of 0.0103° with 5.85 scannings per minute.

4.3.2 SEM-EDS

Scanning Electron Microscopy (SEM) is an imaging technique conducted with an electron microscope to produce an image of the analyzed sample to observe particle sizes, shapes and dispersity. Some electron microscopes, like the one used in this thesis, also have the ability to conduct Energy-dispersive X-ray Spectroscopy (EDS), an analytical method to determine the atomic composition of the material. Both procedures are conducted by the same electron microscope and are therefore grouped together in this thesis. The procedure was conducted on the Zeiss Supra 35VP electron microscope.

4.3.3 Thermogravimetric analysis

Together with PXRD, TGA is also useful to verify the material analyzed, and together they serve to get a comprehensive understanding of the sample quality. When analyzing untreated synthesized MOFs, the amount of solvent and unreacted linkers could also be observed in the TGA plot. The first drop in weight% usually indicates the solvent leaving the material, and the next drop before the main decomposition might indicate if there are unreacted linkers decomposing. The sample is analyzed by placing roughly 10-25 mg of the desired sample in an alumina oxide crucible, then weigh the sample to get the total weight before analysis. The sample is then placed in the TGA apparatus, where the sample is continuously weighed in a controlled environment while the temperature is increased stepwise from 25°C up to the desired temperature, in this case being 800°C. The heating rate of the procedure used is 10°C per minute, with synthetic air used to purge the environment at a rate of 20 ml per minute. The TGA on the samples in this thesis was conducted on a Mettler Toledo TGA/DSC 3+ STARe System, using synthetic air as a purge gas to control the analysis environment.

4.3.4 Sample activation

The degassing system uses a vacuum pump and a heating element with an adjustable temperature setpoint to meet the samples required degassing temperature, with capacity of up to six sample cells. Samples are degassed by attaching a vacuum hose and adapter to the opening of the sample cells, then placed in the heating area after the vacuum has been turned on. The samples used in all sorption analyses were degassed in a Micromeritics VacPrep 061 Sample Degas System as seen in figure 4.1.

4.3.5 N_2/CO_2-sorption

The sorption analysis is conducted to produce pure component isotherm data of the samples, both to calculate material properties such as specific surface area and porosity through N_2 sorption at 77K, and to produce CO_2 and N_2 isotherms at 273K and 293K to analyze different gas adsorption mechanics and gas uptake capacities closer to operating temperatures. The 77K sorption analysis were conducted with sample cooling by liquid nitrogen in a container, while the 273K and 293K were conducted by filling the container with ice water and room temperature water respectively to reach the desired analysis temperature. All N_2 and CO_2 sorption analyses were conducted with a Micromeritics TriStar II, as seen in Figure 4.3.

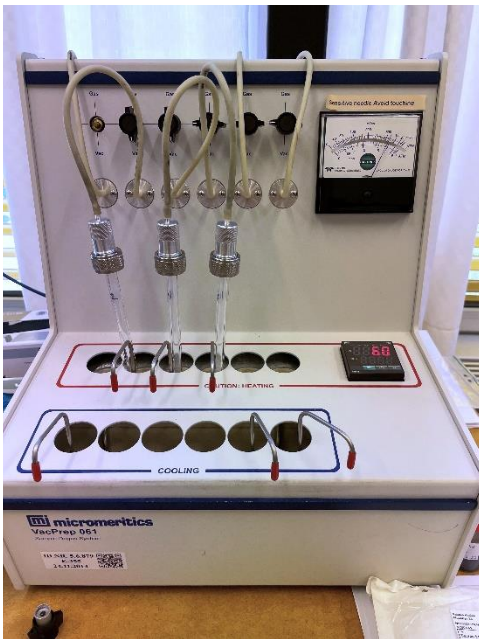

Figure 4.2. Micromeritics VacPrep 061 Vacuum Degas System with three sample cells under degassing at 60°C.

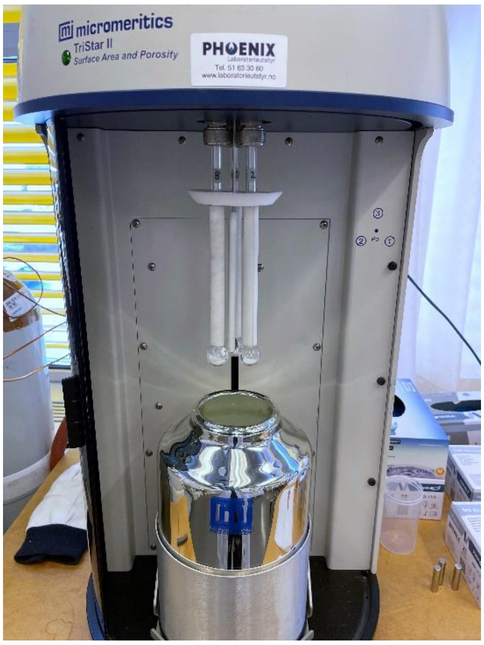

Figure 4.3. Fully loaded Micromeritics TriStar II sorption apparatus used to determine pure component sorption isotherms.

4.3.6 Python calculations

All graphs and calculations presented in this thesis are calculated using Jupyter Notebooks, an open-source software which runs the Python 3 programming language. The scripts written for calculations in this thesis use a range of different python packages. These packages contain useful functions and tools which simplify the calculations needed, and make the script easier to read and modify. The python package Pandas has been used for data loading and the creation of dataframes, Numpy has been used to construct arrays and run numerical methods, Sklearn for regression analysis, and Matplotlib has been used for plotting the data and calculation results. The sample data used for the TGA, BET analysis, adsorption analysis and isosteric heat of adsorption analysis are to be converted to a CSV format and then loaded into a sample class to be able to convert units and make the dataframe accessible for calculations through the script. The python scripts used for the calculations and plots used in this thesis could be found in Appendix A.

The selectivity and adsorbed N2 and CO2 quantities in mixed gas systems obtained in this thesis are calculated using a self-written program programmed in python, assisted with the pyIAST python package. The package uses IAST to predict the gas adsorption isotherms of gas mixtures with two or more components (Simon et al., 2016).

5 Results and discussion

In this section, the synthesis and characterization results are presented and discussed. Specific surface area, porosity, selectivity, and isosteric heat of adsorption are calculated to get an overview of the gas separation properties of the materials analyzed. This will enable us to see how they behave under different process conditions.

5.1 Sample preparation

All synthesized samples, shown in table 5.1, measured a percentage yield higher than 100%, which is most likely caused by some degree of moisture and unreacted linkers contained in the samples, as the weight measurements were conducted directly after air-drying. The samples analyzed that were not synthesized, including samples with washing treatments and an outsourced zeolite-13X sample are listed in table 5.2.

Sample name/nr.	Metal source Mol Eq.	Linker Mol Eq.	Solvent Mol Eq.	Modulator Mol Eq.	Theoretical yield (g)	Actual yield (g)	Product description	Reaction time	Reaction temp. °C
MIP-202-01	$ZrCl_4$:1	Aspartic acid :2.091	Water :56	-	3.6167	3.6568 101.1%	White powder	24 h	120
MOF-801-02	$ZrCl_4$:1	Fumaric acid :1	Water :138	Acetic acid :43.7	1.1364	1.5257 134.26%	White powder	20 h	95
Ce-MIP-202-04	CAN :1	Aspartic acid: 1.5	Water :	Formic acid:	1.4106	1.5257 108.2%	Yellow powder	0.5 h	100

Table 5.1. Synthesis results of MIP-202, MOF-801 and Cerium based MIP-202.

Sample name/nr.	Treatment	Product description
MOF-801-03	Wash with Acetic acid	White powder
Zeolite-13X-05	-	White powder
MIP-202-06	Wash with methanol	White powder
Ce-MIP-202-07	Wash with methanol	Yellow powder
Ce-MIP-202-08	Wash with Acetic acid	Yellow powder
MOF-801-09	Wash with NaAc	White powder

Table 5.2. Other samples used in the thesis, including outsourced samples and sample washings.

5.2 Powder X-ray diffraction

5.2.1 PXRD of untreated samples

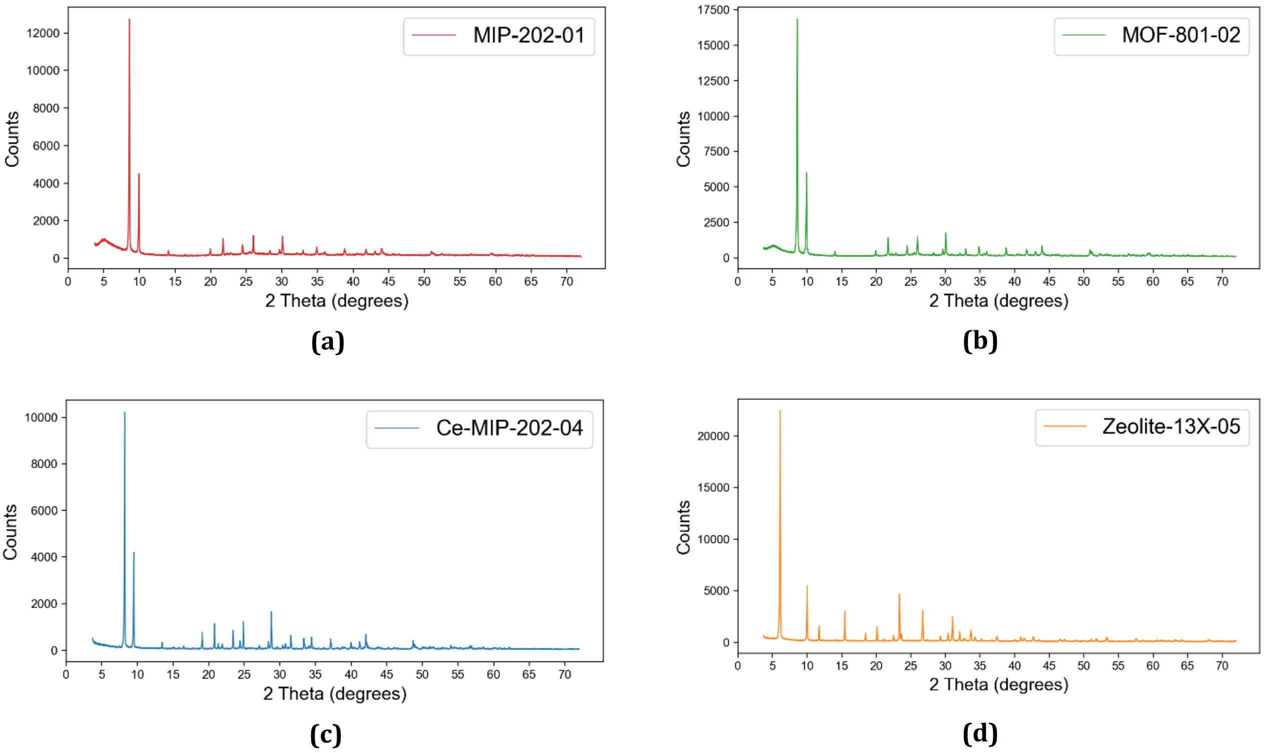

(a)

(b)

(c)

(d)

Figure 5.1. Post synthesis PXRD patterns for (a) MIP-202-01, (b) MOF-801-02, (c) Ce-MIP-202-04, (d) Zeolite-13X-05.

All synthesized samples were analyzed with PXRD and plotted with angle 2θ on the x-axis and counts on the y-axis, as shown in figure 5.1. All untreated samples exhibit clear and sharp peaks, which are indications of a highly crystalline material. The peaks of the MIP-202-01 sample match well with the PXRD data reported in (Wang et al., 2018), as do the peaks of MOF-801-02 compared to the ones reported in (Jahan et al., 2022). The Zeolite-13X-05 sample also exhibits sharp peaks as expected from an outsourced product, and displays the correct peak similarity compared to the one reported in (Masika & Mokaya, 2013). PXRD results of all untreated MOFs provide high levels of assurance that the correct MOFs were synthesized with desired crystallinity and structure, hence the samples were subjected to sample washings and TGA analysis for further measurements.

5.2.2 PXRD of treated samples

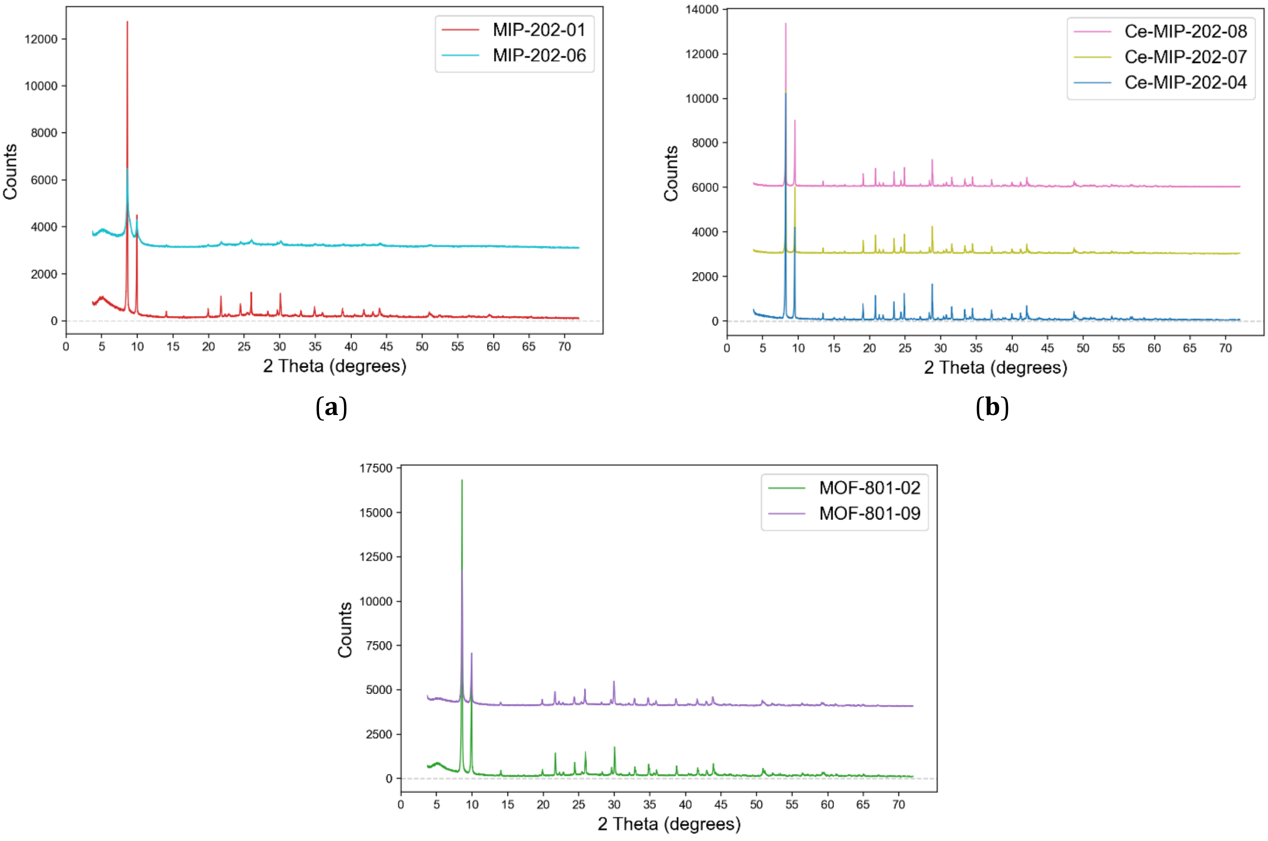

(a)

(b)

(c)

Figure 5.3. Comparison of PXRD patterns of (a) MIP-202-01/06, (b) Ce-MIP-202-04/07/08, and (c) MOF-801-02/09.

The results from the PXRD of the washed samples determine if the crystalline structure and integrity of the MOF has been retained through the washing procedure. As seen in figure 5.3.a, the methanol washed MIP-202-06 sample has a significant reduction in intensity of the spikes compared to the untreated MIP-202-01, clearly indicating a damaged MOF structure as a result of the washing. The methanol washed Ce-MIP-202-07 and the acetic acid washed Ce-MIP-202-08, shown in figure 5.3.b, both exhibit a slight reduction in intensity compared to the untreated Ce-MIP-202-04, however the change does not seem to have caused a loss of structure. The PXRD of the sodium acetate wash MOF-801-09 shown in figure 5.3.c also indicates that the MOF-801-02 sample retains its structure and crystallinity reasonably well.

5.3 SEM-EDS

5.3.1 Scanning electron microscopy

Scanning electron microscopy (SEM) was conducted to analyze the morphology of MIP-202-01, MOF-801-02 and Ce-MIP-202-04. Figure 5.4.a shows the micrograph of MIP-202-01, where the particle sizes lie between 200-600 nm with non-uniform appearance and low dispersity. This corresponds well to the particle size distribution reported in literature, where particle sizes ranged between 95 to 652 nm (Diab, Salama, Hassan, Abd El-moneim, et al., 2021). The particle size of MOF-801-02 appears to lay around 200 nm from observation of figure 5.4.b. The particles also show good dispersity and a relatively uniform particle size, which is expected as the same observations were reported in (Ke et al., 2018). The Zeolite-13X-05 particles shown in figure 5.4d show particle sizes between 200-500 nm, with high dispersity and uniform particle size.

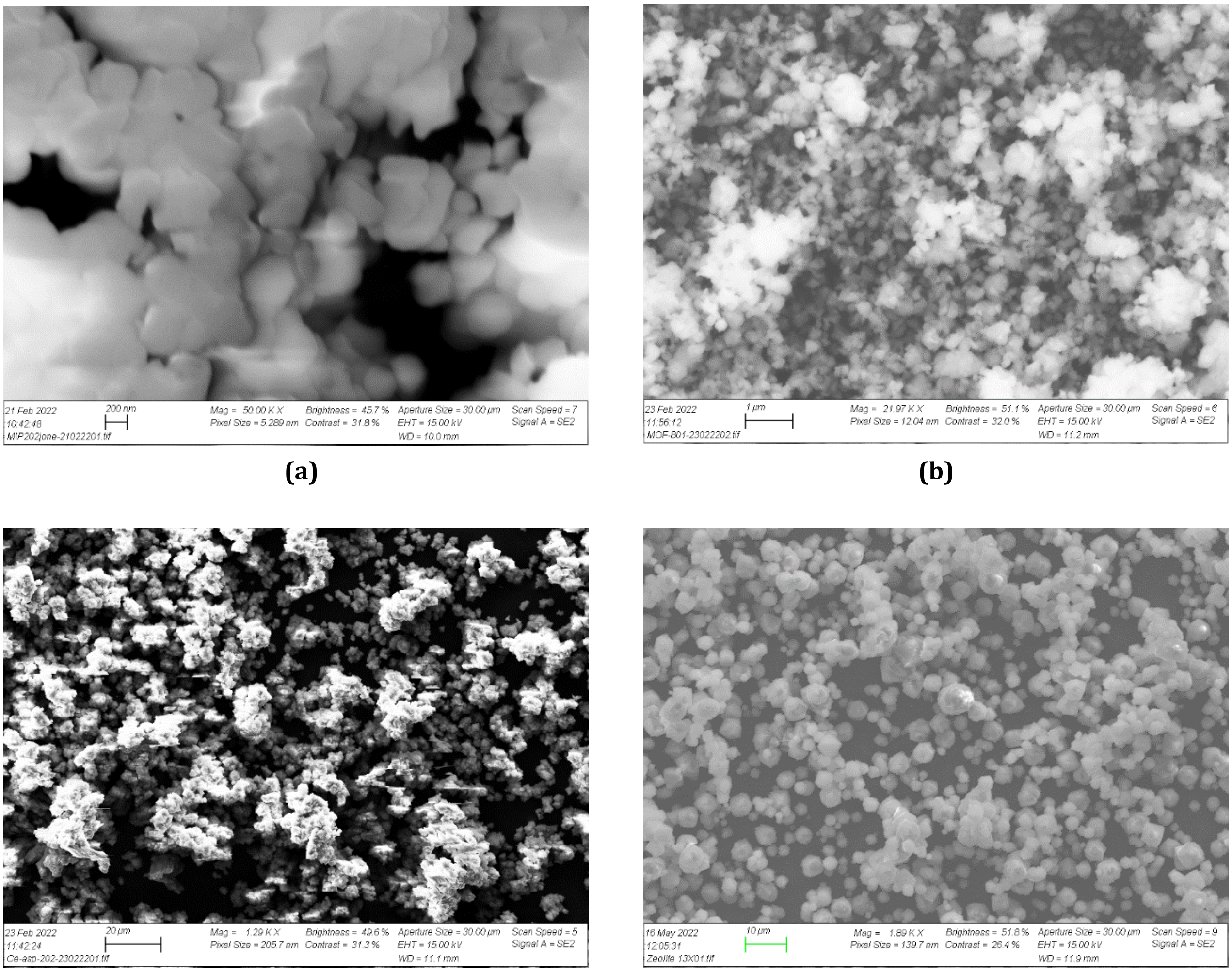

(a) **(b)**

(c) **(d)**

Figure 5.4. SEM micrographs of (a) MIP-202-01, (b) MOF-801-02, (c) Ce-MIP-202-04, and (d) Zeolite-13X-05.

5.3.2 Energy-dispersive X-ray spectroscopy

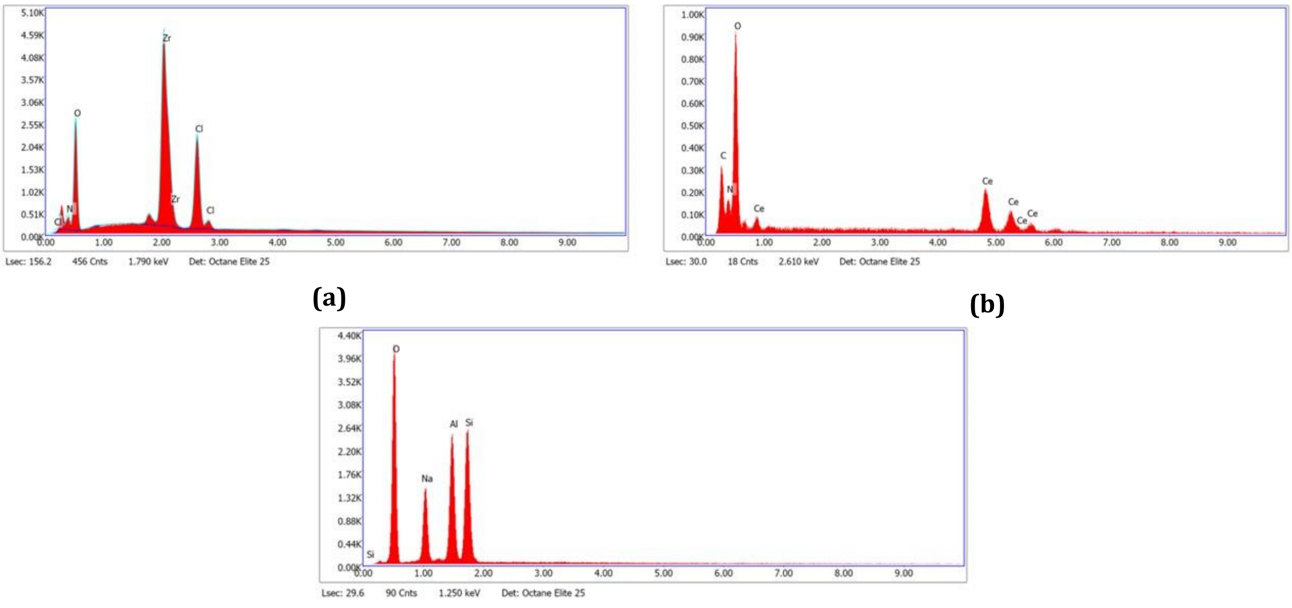

(a)

(b)

(c)

Figure 5.5. EDS spectrum of (a) MIP-202-01, (b) Ce-MIP-202-04, (c) Zeolite-13X-05

The EDS spectrum of MIP-202-01 illustrated by figure 5.5.a, indicates that there is a substantial amount (17.83 wt%) of chloride ions present in the sample, despite there being no chloride ions in the MIP-202 formula. The same phenomenon is also seen in the MOF-801 EDS shown by figure 5.6, but to a lesser degree (5.51 wt%). The chloride ions are likely to have originated from the ZrCl4 the MOF was synthesized with. It has been hypothesized that the chloride ions could block the pores of the MOF, decreasing the gas loading capacity, and that MIP-202 has the higher chloride content of the two, due to binding of chloride ions to the amine groups on the aspartate linkers. In comparison to MIP-202-01 and MOF-801-02, the EDS plot for the cerium-based MIP-202 shows no sign of chloride ions as seen in figure 5.5b, which is expected since the Ce-MIP-202-04 sample was not synthesized with a chloride containing salt.

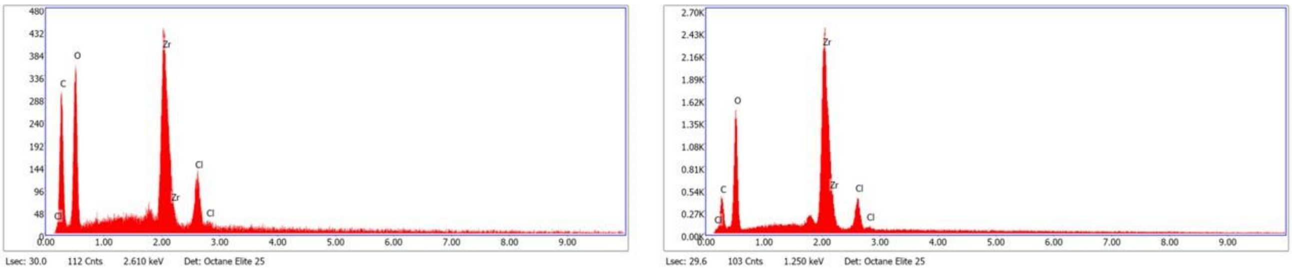

Figure 5.6. EDS spectrum of MOF-801-02 (Left) and MOF-801-03 (Right).

The chloride content of the washed MOF-802-03 sample, shown to the left in figure 5.6, does not seem to have been affected to a desired degree, as the weight percentage of chloride ions has only increased from 5.51 wt% to 5.35 wt%. There is however a substantial reduction in detected carbon atoms, where the reduction from 39.46 wt% to 18.51 wt% is too large to be explained by the possible removal of excessive linkers from the product. The MOF-801-03 was the only treated MOF sample to be analyzed with SEM/EDS due to limited time. The complete EDS table data is available in Appendix B.

5.4 Thermogravimetric analysis

5.4.1 TGA of untreated samples

The sample weight data from the TGA is normalized to weight% at the temperature endpoint of the analysis, where 100% is the weight% of the metal oxide end product after reaching 800°C. The TGA analysis is also a helpful tool to use when determining the optimal temperature at which the samples could be degassed without decomposing, however detecting possible MOF structure failure excepting decomposition is not possible with the information given solely by the TGA graph.

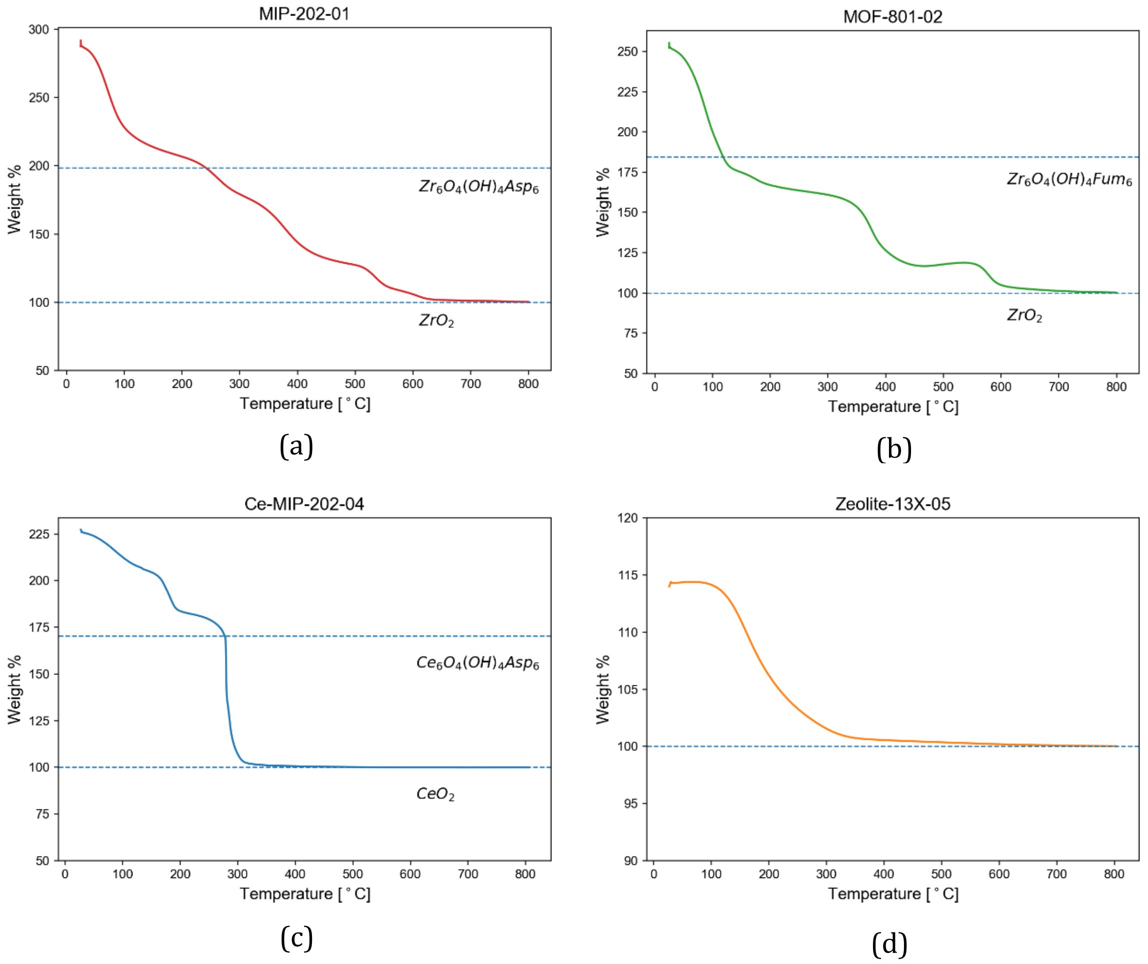

(a) (b) (c) (d)

Figure 5.7. TGA graphs for (a) MIP-202-01, (b) MOF-801-02, (c) Ce-MIP-202-04, (d) Zeolite-13X-05

The TGA curve of the Zeolite-13X-05 sample, seen in figure 5.7.d, only demonstrates the loss of moisture on the temperature range between 25-800°C, this is expected as Zeolite-13X has been shown to be stable up 1000°C (Masika & Mokaya, 2013). The TGA curve of Zeolite-13X-05 also demonstrates that it needs a high activation temperature to be fully activated before gas sorption experiments. This is because the weight of the sample does not stabilize before above 300°C.

The theoretical weight of the MOFs relative to the weight of the metal oxide products, was calculated and plotted onto the TGA plots, by dividing the molar mass of each MOF by the molar mass of the metal oxide end product, with the correct stoichiometric coefficients from each reaction. The theoretical weight percentages of the MOFs and their respective metal oxides were plotted as dashed lines in the TGA plots. The weight percentages were calculated by the following equations, where the theoretical weight% for MIP-202 in relation to its end products is calculated in equation 5.1, MOF-801 in equation 5.2, and Ce-MIP-202 in equation 5.3:

$$\frac{Zr_6O_4(OH)_4Asp_6}{6\,ZrO_2}\cdot 100\% = \frac{1465.9\ g/mol}{6\cdot 123.22\ g/mol}\cdot 100\% = 198.3\% \tag{5.1}$$

$$\frac{Zr_6O_4(OH)_4Fum_6}{6\,ZrO_2}\cdot 100\% = \frac{1363.7\ g/mol}{6\cdot 123.22\ g/mol}\cdot 100\% = 184.5\% \tag{5.2}$$

$$\frac{Ce_6O_4(OH)_4Asp_6}{6\,CeO_2}\cdot 100\% = \frac{1759.3\ g/mol}{6\cdot 172.12\ g/mol}\cdot 100\% = 170.4\% \tag{5.3}$$

5.4.2 TGA of washed samples

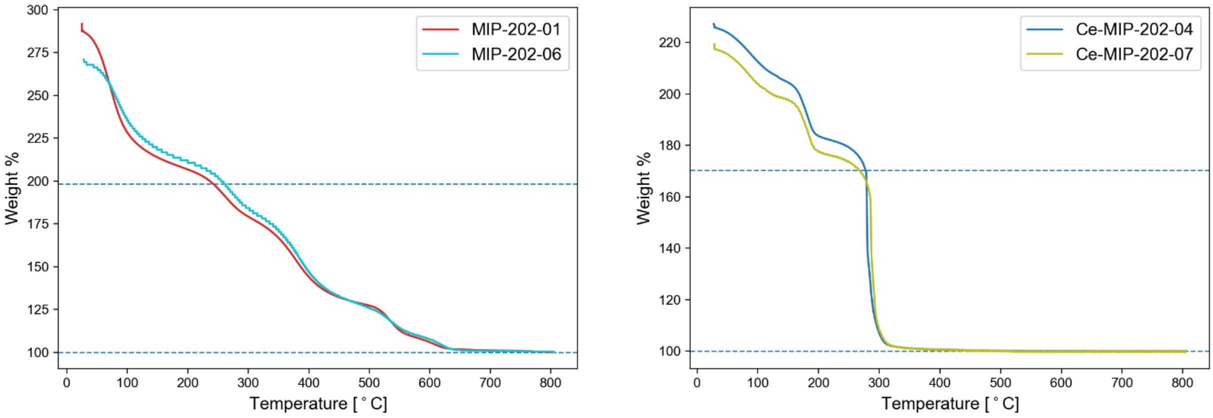

Figure 5.8. (**Left**) TGA comparison plot of MIP-202-01 and MIP-202-06. (**Right**) TGA comparison plot between Ce-MIP-202-04 and Ce-MIP-202-07

In the comparison plot between the MIP-202-01 sample and the methanol washed MIP-202-06 sample shown in figure 5.8 to the left, there is no significant difference between the TGA graphs between the two samples, other than the first mass drop around 50-100 °C, which could be explained by a lower solvent content in the methanol washed sample. From figure 5.8 to the right, we can see that the last mass drop at 300 °C is somewhat different for the Ce-MIP-202-04 sample and the methanol washed Ce-MIP-202-07 sample, which loses a lower weight% compared to the unwashed sample. The rest of the graphs do not indicate any significant difference. Both the MIP-202 and the cerium-based MIP-202 should have the same structure and consist of the same linker, however the thermal decomposition as seen in the TGA graphs shows significant differences.

5.5 Specific surface area and porosity

The specific surface area and porosity (pore volume) of the synthesized MOFs and the Zeolite sample was calculated by using the Brunauer–Emmett–Teller (BET) model with the data collected from the 77K nitrogen sorption analysis of the selected samples. The theory is widely used for calculating the specific surface area and total pore volume of microporous materials. It is an extended adsorption model of the Langmuir model, which only considers the monolayer adsorbed quantity of gas.

$$\frac{1}{V\left((P^0/P)-1\right)} = \frac{C-1}{V_m \cdot C}\left(\frac{P}{P^0}\right) + \frac{1}{V_m \cdot C} \tag{5.4}$$

The isotherm data points used for the BET plot are collected between a relative pressure range between 0.05 and 0.35, as this is the region displaying the best linear relation between the axes. The procedure and equations for calculating BET surface area and total pore volume were collected in (Galarneau et al., 2018). By plotting the left-hand side of equation 5.4 on the y-axis and the relative pressure on the x-axis using the experimental data, the monolayer pore volume (V_m) of the equation could now be calculated by finding the slope (β) and intercept (α) of the linear equation constructed by linear regression of the data points. The monolayer pore volume and the BET surface area (S_{BET}) are determined by solving the following equations with the linear regression coefficients:

$$V_m = \frac{1}{\beta + \alpha} \tag{5.5}$$

$$S_{BET} = \frac{\sigma_{N2} \cdot V_m \cdot N_A}{V_{N2}} \tag{5.6}$$

Where σ_{N2} is the cross-sectional area of the N_2 molecule, taken as 0.162 nm^2 from (Saidi et al., 2021). V_m is the monolayer volume found in equation 5.5, N_A is Avogadro's number, defined as approximately 6.022×10^{23}, and V_{N2} is the molar gas volume for N_2 at STP, corresponding to 22.4×10^3 cm^3. All terms in equation 5.6 except the monolayer pore volume are physical constants when inserted for N_2, therefore equation 5.6 could be simplified in each case of N_2 sorption at 77K to a more applicable function of only the monolayer pore volume by the following equation:

$$S_{BET}(m^2/g) = 4.355 \cdot V_m(cm^3STP) \tag{5.7}$$

The total pore volume of the sample is calculated with the following formula, where the number 694 is the expansion ratio of N_2 between liquid and gas, and n_m is the adsorbed amount of nitrogen at a relative pressure of 0,5.

$$V_T = \frac{n_{m,@0.5}}{694} \tag{5.8}$$

All MOF samples were degassed at 60°C for 24 hours under vacuum before the first 77K N_2 sorption analysis, then 2 hours between each subsequent CO_2/N_2 analysis with the same samples. All sorption measurements were conducted with around 100 mg of adsorbent. However, only the MOF-801 samples showed satisfactory results after 60°C activation. The Zeolite-13X-05 sample was activated at 350°C for 2 hours. Therefore, the MIP-202-01, MOF-801-02 and Ce-MIP-202-04 samples were degassed at 120°C for 24 hours and analyzed again. The Ce-MIP-202-04 sample underwent an apparent color change during degassing at 120°C, giving the sample a darker yellow color as seen in figure 5.9, which could be a sign of degradation.

Figure 5.9. Ce-MIP-202-04 sample in an analysis cell before (right) and after (left) degassing at 120°C.

The 77K Nitrogen sorption isotherms for MIP-202-01/06 and Ce-MIP-04/07/08, illustrated in figure 5.10, deviated substantially from the expected data, and were therefore considered unusable for sensical BET surface area calculations and further sorption analysis. A systematic machine error was highly unlikely as some of these samples were measured alongside the MOF-801 samples which gave satisfactory results, changing between machine ports between measurements. The N_2 uptake of MIP-202 reported in (Saidi et al., 2021) stabilized at around 100 cm^3g^{-1} STP, while the uptake measured on the MIP-202-01 sample stabilized at around 5 cm^3g^{-1} STP, which is drastically lower. The Ce-MIP-202-04/07/08 all gave isotherms with negative values, which could be caused by a combination of insufficient sample quantity analyzed and a very low general N_2 uptake on the Ce-MIP-202 samples.

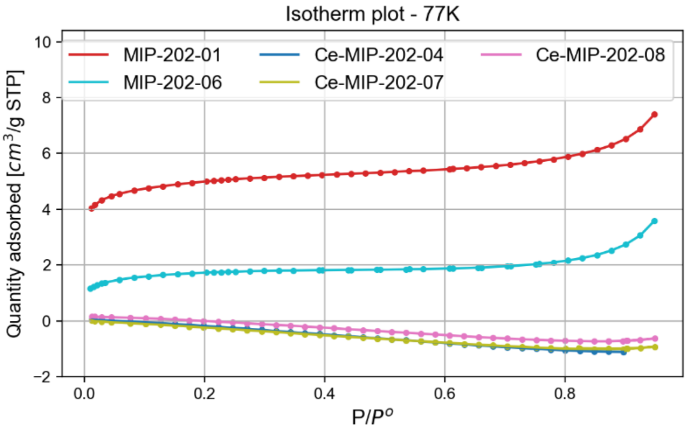

Figure 5.10. 77K Nitrogen sorption isotherms of the MIP-202-01/06 and Ce-MIP-04/07/08.

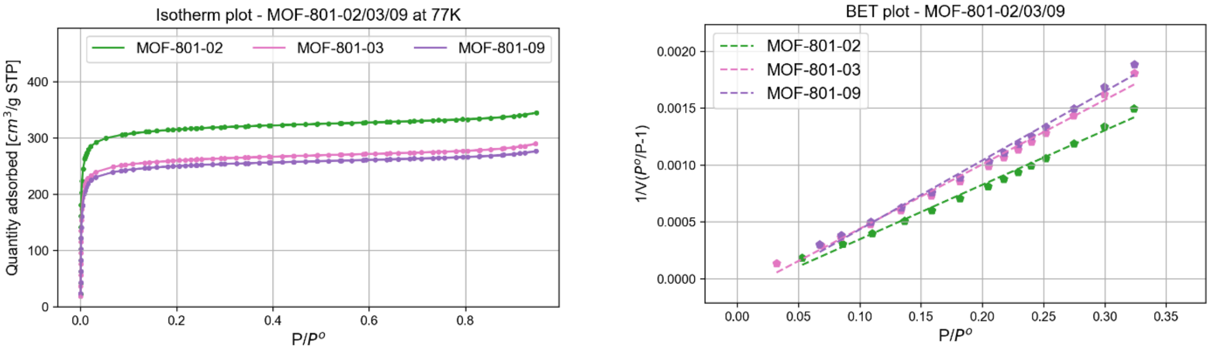

Figure 5.11: (**Left**) 77K Nitrogen sorption isotherms for MOF-801-02 (Green), MOF-801-03 (Pink), MOF-801-09 (Purple), all degassed at 60°C. (**Right**) BET transform plot of the corresponding MOF-801 samples.

The 77K sorption isotherms for the MOF-801 samples shown in figure 5.11 indicate that the adsorptivity has decreased after washing treatments, as the untreated MOF-801-02 samples have a significantly higher N_2 uptake compared to MOF-801-03 and MOF-801-09, which was washed with acetic acid and sodium acetate respectively. The adsorptivity decrease is also reflected in the BET surface area and total pore volume seen in table 5.3. The BET surface area and total pore volume of MOF-801 reported in literature are 755 m^2g^{-1} and 0.44 cm^3g^{-1} respectively, which both lies between the calculated surface area of the MOF-801-02 samples measured after 60°C and 120°C degassing for 24 hours (Ke et al., 2018). A defect in the pore structure may be responsible for the high surface area of the MOF-801 samples, as this could increase pore size, further increasing the adsorptivity, as reported in (Saidi et al., 2021).

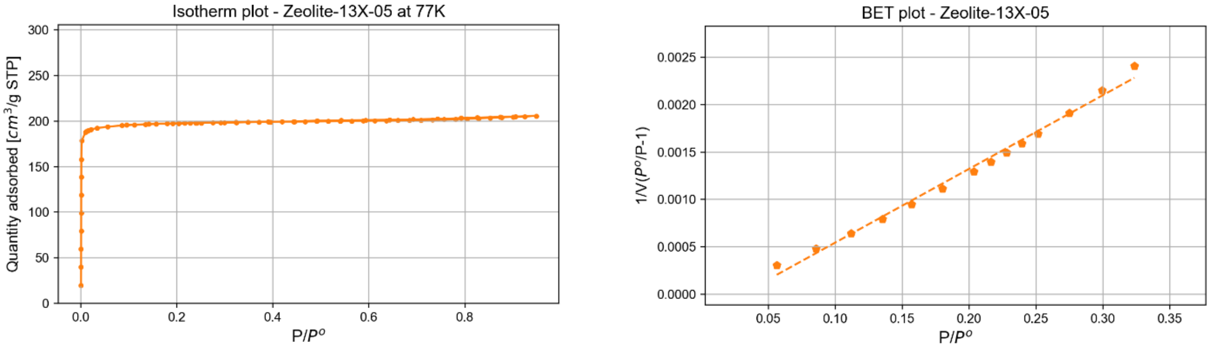

Figure 5.12. (**Left**) 77K Nitrogen sorption isotherms for Zeolite-13X-05. (**Right**) BET plot for Zeolite-13X-05.

The Zeolite-13X-05 N_2 at 77K isotherm shown in figure 5.12, displays a sharp adsorption curve that stabilizes quickly around 200 cm^3g^{-1} STP. The N_2 uptake, BET surface area of 577.7 m^2g^{-1}, and the total pore volume of 0.2963 cm^3g^{-1} which are presented in table 5.3, all compare well to the data in (Mfoumou et al., 2018), which reported a BET surface area of 590 m^2g^{-1} and a total pore volume of 0.317 cm^3g^{-1}.

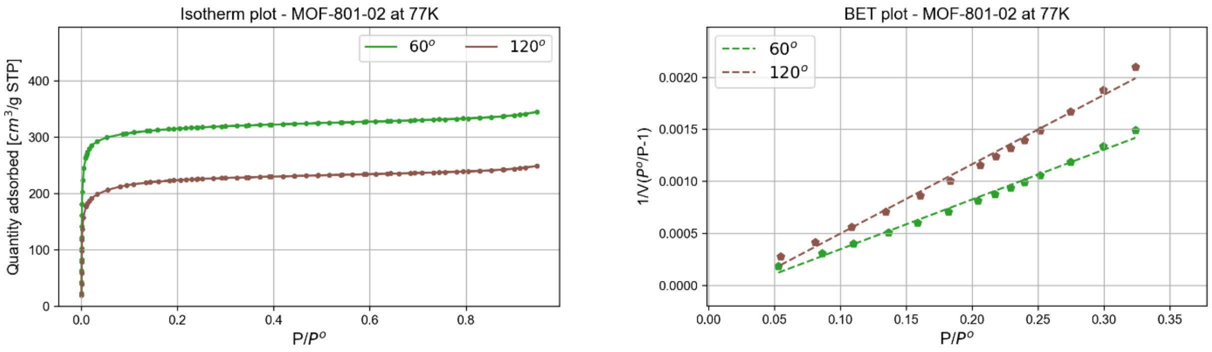

Figure 5.13. (**Left**) 77K Nitrogen sorption isotherms for MOF-801-02 degassed at 60°C and 120°C. (**Right**) BET transform plot of the corresponding MOF-801-02 sample.

The 77K sorption analysis of the samples degassed at 120°C did not yield any significant different or valid results for MIP-202-01 and Ce-MIP-202-04. The rest of the adsorption analyses for these samples were therefore discontinued. The 77K N_2 sorption isotherms for MOF-801-02 after the 120°C degassing did however give good results as seen in figure 5.13, but had a lower N_2 uptake compared to the sample analyzed after 60°C degassing.

Sample name	**BET surface area [m^2/g]**	**Total pore volume [cm^3/g]**	**Monolayer pore volume [cm^3/g]**	**BET plot R^2**
MOF-801-02 at 60°C	936.5	0.4683	214.8	0.9911
MOF-801-02 at 120°C	670.7	0.3349	153.8	0.9911
MOF-801-03 at 60°C	787.4	0.4172	180.6	0.9910
MOF-801-09 at 60°C	739.9	0.3985	169.7	0.9921
Zeolite-13X-05 at 350°C	577.7	0.2963	132.5	0.9908

Table 5.3: BET surface area, total pore volume, and monolayer pore volume calculated by the BET plot parameters and equation 5.5, 5.7, and 5.8.

Both the MOF-801 and Zeolite-13X samples show a steep adsorption curve at low pressures and stabilize quickly. The nitrogen sorption isotherms collected from the samples which showed satisfying results, all show type I isotherms as seen to the left in figures 5.11, 5.12 and 5.13, which is expected for microporous materials. The BET transform plots, BET surface area, total pore volume and monolayer pore volume were all calculated by the python script in appendix A.5.

5.6 CO_2/N_2 Separation

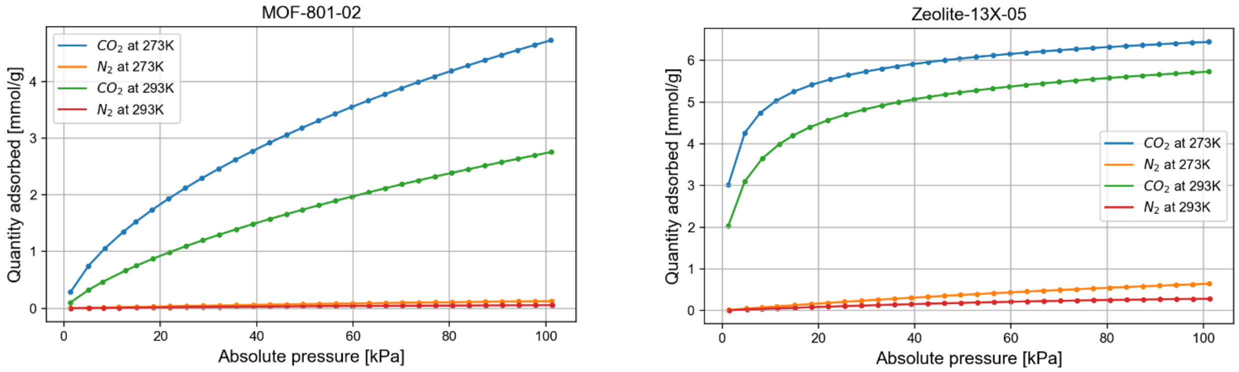

Figure 5.14. CO_2 and N_2 pure component adsorption isotherms for MOF-801-02 (Left) and Zeolite-13X-05 (Right) at 273K and 293K measured by the Micromeritics Tristar II.

The CO_2/N_2 adsorption analysis where then executed both at 0°C and 20°C. All test results show a relatively large drop in adsorbed amount on all samples, which is to be expected as higher temperatures decrease adsorptivity of the adsorbent. The MOF-801-02 CO2 isotherms shown to the left in figure 5.14 respond to the change in temperature to a greater degree than that of Zeolite-05-13X , shown to the right. This could be favorable when using temperature-swing adsorption, but could be disadvantageous if the process runs at a high temperature due to a low uptake of CO2.

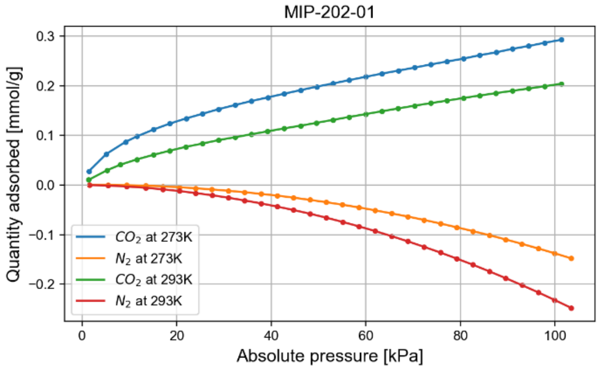

Figure 5.15. CO_2 and N_2 pure component adsorption isotherms for MIP-202-01 at 273K and 293K measured by the Micromeritics Tristar II.

The N_2 adsorption isotherms for MIP-202-01 shown in figure 5.15, has most likely negative values due to a low sample amount analyzed combined with the sample's low uptake. The uptake of 0.29 mmol g^{-1} CO_2 for the 273K isotherm at 100 kPa is considerably low compared to MIP-202 samples reported in (Skjærseth, 2021), which has a reported uptake of 1.38 mmol g^{-1} for the MIP-202 synthesized with DL-aspartic acid.

5.7 Ideal adsorbed solutions theroy

5.7.1 CO2/N2 Coadsorption

Ideal Adsorbed Solution Theory (IAST) is a theoretical model used to predict gas co-adsorption when dealing with gas mixtures with two or more components, by utilizing each gas-component's individual adsorption isotherm. The model assumes that the structure of the MOF stays fixed during adsorption, thus making the model inaccurate for flexible materials with "gate-opening" behavior. (Fraux et al., 2018). The equations below are solved for P_A^* and P_B^*, used in the proceeding calculations.

$$\int_0^{P_A^*} \frac{n_A(p)}{p} \mathrm{d}p = \int_0^{P_B^*} \frac{n_B(p)}{p} \mathrm{d}p \tag{5.9}$$

Where $n_A(p)$ and $n_B(p)$ are the functions of the individual isotherms of each gas. The integrals can either be solved with numerical integration from the experimental data, or solved analytically by integration using a fitted isotherm model to the data (Fraux et al., 2018). The fractions of the adsorbed quantities of each gas can then be determined by using the obtained P_A^* and P_B^* values from the integrals with the formula below:

$$x_i = \frac{p_i}{P_i^*} \tag{5.10}$$

Selectivity can then be calculated from the predicted adsorbed quantities received from IAST model, and the partial pressure of the components by using the equation below, where S_{ads} is selectivity, x_A and x_B are the fractions of the adsorbed gases, and where p_A and p_A is the partial pressure of the gases.

$$S_{ads} = \frac{x_A}{p_A} \cdot \frac{p_B}{x_B} \tag{5.11}$$

IAST gas coadsorption and selectivity analysis were conducted on the MOF-801-02 and the Zeolite-13X sample. For the MOF-801, a Langmuir model (Equation 5.12) was used to model the CO2 and N2 isotherms from the experimental data. The Zeolite-13X-05 was modelled with a dual-site Langmuir isotherm model (Equation 5.13) for the CO2 isotherms, and Henry's adsorption isotherm (Equation 5.14) for the N2 isotherms. The K and M variables in the isotherm models described by equation 5.12 to 5.14 are fitting parameters, n(p) is the quantity adsorbed as a function of the pressure p.

$$n(p) = M \cdot \frac{K \cdot p}{1 + K \cdot p} \tag{5.12}$$

$$n(p) = M_1 \cdot \frac{K_1 \cdot p}{1 + K_1 \cdot p} + M_2 \cdot \frac{K_2 \cdot p}{1 + K_2 \cdot p} \tag{5.13}$$

$$n(p) = K_H \cdot p \tag{5.14}$$

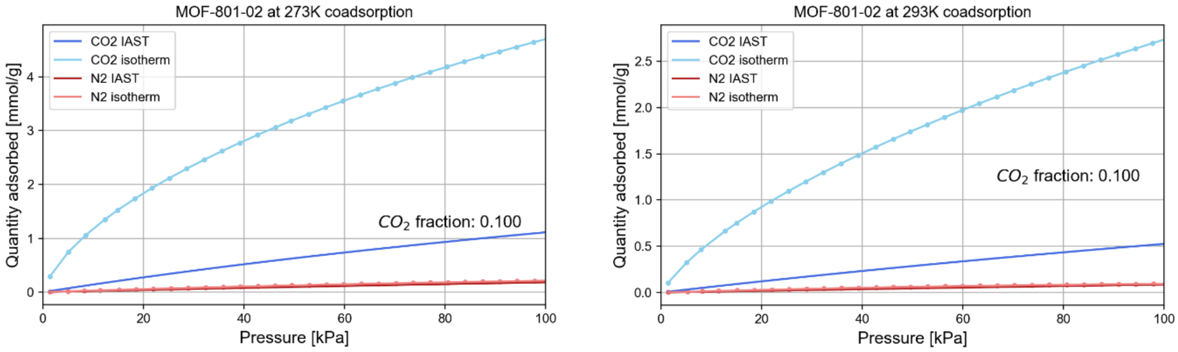

Figure 5.16. CO_2/N_2 coadsorption loadings on MOF-801-02 with a gas mixture of 10 mole% CO_2 and 90 mole% N_2 at 273K (Left) and 293K (Right).

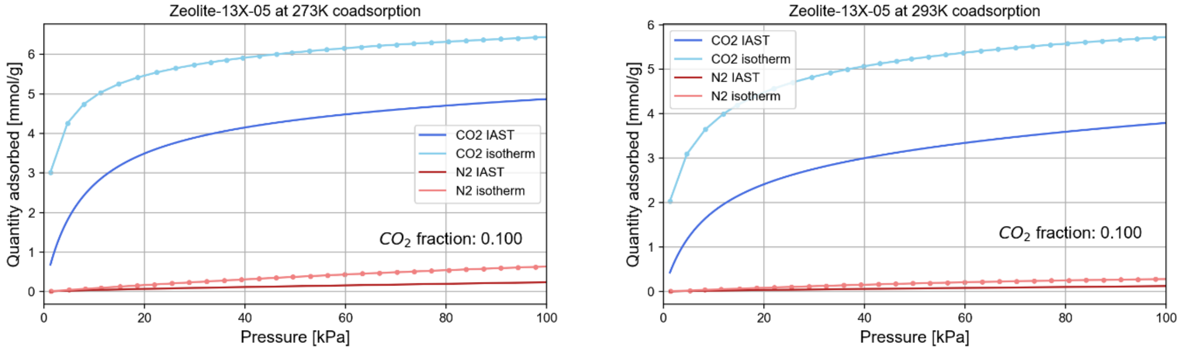

Figure 5.17. CO_2/N_2 coadsorption loadings on Zeolite-13X-05 with a gas mixture of 10 mole% CO_2 and 90 mole% N_2 at 273K (Left) and 293K (Right).

The plots in figures 5.16 and 5.17 describe the adsorbed amounts when CO2 and N2 are in a mixture, also called coadsorption. The lower predicted CO2 quantity adsorbed is explained by the lower CO2 partial pressure due to the mole fraction 0.10. The effective partial pressure of CO2 at 100 kPa absolute pressure is therefore 10 kPa. Quantity adsorbed of CO2 by the Zeolite-13X-05 is therefore significantly higher in the lower pressure regions due to the high value on the Zeolite isotherm at 10 kPa. When the partial pressures are considered, we see that the reduction in N2 adsorbed on Zeolite-13X-05 is reduced by 56-60%, which is significantly less than the adsorbed amount at 90 kPa, as seen in table 5.4. This is expected as the CO2 molecules are favorable for adsorption and occupies the pore structure at lower pressures. It does not however seem like the percentage reduction in N2 adsorbed on the MOF-801 is reduced in a larger degree than CO2. It also seems that the percentage reduction is slightly higher at 273K compared to 293K.

Sample and gas type	Pure component loading (mmol g^{-1}) 273K/293K	IAST loading (mmol g^{-1}) 273K/293K	Percentage reduction in loading at equal partial pressure 273K/293K
MOF-801-02 CO_2	1.192/0.592	1.110/0.526	7%/11%
MOF-801-02 N_2	0.205/0.094	0.182/0.086	11%/9%
Zeolite-13X-05 CO_2	4.923/3.851	4.871/3.792	3%/2%
Zeolite-13X-05 N_2	0.618/0.288	0.238/0.123	60%/56%

Table 5.3. Differences in experimental gas loadings compared to predicted loadings by IAST on MOF-801-02 and Zeolite-13X-05, where the pure component loading of CO_2 is taken at 10 kPa, N_2 at 90 kPa and IAST loading at 100kPa.

5.7.2 Selectivity

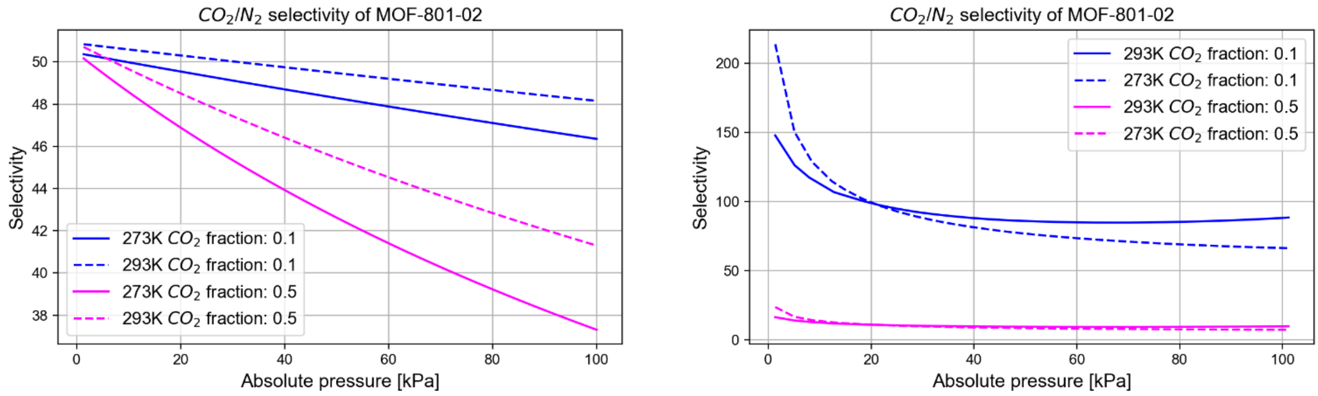

Figure 5.18. IAST CO_2/N_2 adsorption selectivity plot for MOF-801-02 at 293K and 273K. (**Left**) Selectivity at different absolute pressures at 0.1 and 0.2 CO_2 mole fractions, (**Right**) Calculated selectivity directly from the isotherm data of MOF-801-02 using formula 5.11.

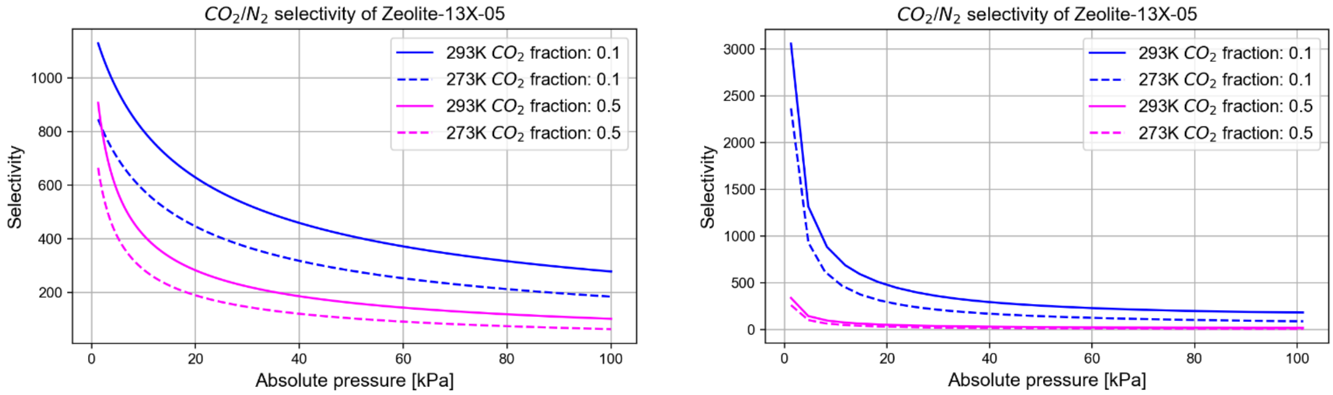

Figure 5.19. IAST CO_2/N_2 adsorption selectivity plot for Zeolite-13X-05 at 293K and 273K. (**Left**) Selectivity at different absolute pressures at 0.1 and 0.2 CO_2 mole fractions, (**Right**) Calculated selectivity directly from the isotherm data of Zeolite-13X-05 using formula 5.11.

The MOF-801-02 sample exhibits a relatively stable selectivity profile between 0 and 100 kPa, especially at lower CO_2 fractions From observation of figures 5.18 and 5.19, it appears that the selectivity decreases much slower as the CO_2 fraction of the gas rises in the IAST calculated selectivity compared to the direct calculations from the pure-component isotherm loadings.

The Zeolite-13X-05 exhibits a very high selectivity at lower pressures then decreases rapidly. This is expected as the adsorbed amount at lower pressures is high for Zeolites, as shown in figure 5.19. In figure 5.14 we see that the relative drop in adsorbed gas for N2 is larger than that of CO2 when the temperature is increased from 273K to 293K for the whole isotherm, explaining why the selectivity are lower at lower temperatures for MOF-801-02 and Zeolite-13X-05, shown in figure 5.19 and 5.18 respectively. The selectivity also increases as the mole fraction of CO2 decreases. The same phenomenon is confirmed in (Wei et al., 2017).

5.8 Isosteric heat of adsorption

The isosteric heat of adsorption determines the change in enthalpy as the CO2 or N2 gas is being adsorbed into the adsorbent, in this case being the MOFs and Zeolite-13X. The isosteric heat of adsorption is an important parameter when designing large scale adsorption processes. This is because the heat being released under the adsorption process will decrease the adsorptivity of the adsorbent as the temperature of the system will rise over time. The isosteric heat of adsorption can either be calculated by using a calorimeter or by using the pure component adsorption isotherms at two or more different temperatures, using Equation 5.15, which is derived from the Clausius-Clapeyron equation. The equation assumes that the gases behave ideally and that the volume of the gas adsorbed is negligible relative to the gas phase (Tun & Chen, 2021).

$$Q_{st} = RT^2 \left(\frac{\partial ln(p)}{\partial T} \right)_{ns} \tag{5.15}$$

The isosteric heat of adsorption of the samples was measured by using the pure gas isotherms measured at 273K and 293K respectively. The graphs for the heat of adsorption were collected by fitting the isotherm data from each temperature to a Langmuir model, and collecting the pressure values for the isotherms associated with different loading values. The heat of adsorption is usually found by calculating the slope between the pressure values at each quantity point on a chart where the inverse of the temperature is plotted against the natural logarithm of the absolute pressure, however there is an easier way to calculate the heat of adsorption when dealing with only two isotherms, stated in (Giraldo et al., 2019). Values for heat of adsorption for each quantity point were therefore calculated with equation 5.16, where T_1 is 293K, T_2 is 273K, and p_1 and p_2 are the pressure at each quantity adsorbed gas for the 293K and 273K isotherms respectively. This model was tested up against the previously mentioned technique, both giving the same results, thus confirming the equation.

$$Q_{st} = \frac{R \cdot T_1 \cdot T_2}{(T_2 - T_1) \cdot \ln{(p_1/p_2)}} \tag{5.16}$$

The following isosteric heat of adsorption plots are calculated and graphed using the Python script found in Appendix A.7. The script fits the 273K and 293K pure component isotherm data to an isotherm model using pyIAST. The script then creates two corresponding isotherm functions to get isotherms with more adsorbed quantity data points. The different pressures of each isotherm at the same adsorbed amount are then found and used in equation 5.16 to obtain the isosteric heat of adsorption at the quantity adsorbed. The heat of adsorption points gained by the equation is then plotted on the y-axis and the corresponding adsorbed quantities on the x-axis.

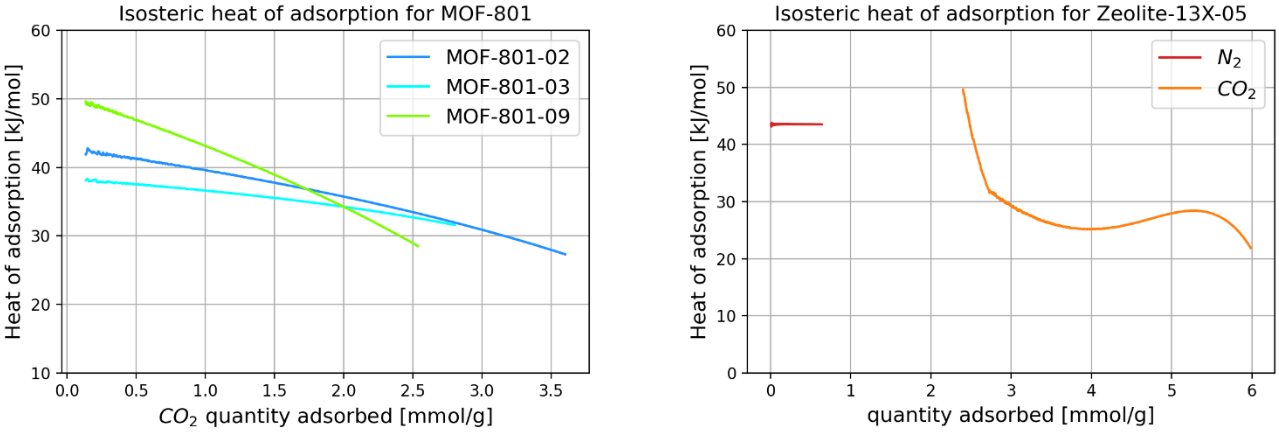

Figure 5.20. (**Left**) CO_2 isosteric heat of adsorption curves for MOF-801-02, MOF-801-03 and MOF-801-09, (**right**) CO_2 and N_2 isosteric heat of adsorption curve for Zeolite-13X-05. Calculated by formula 5.16.

The CO_2 isosteric heat of adsorption calculated for the MOF-801-02/03/09 gave somewhat similar results, with some differences in curve steepness. The heat released by the MOF-801-02 starts at around 42 KJ mol^{-1} at lower loadings, and decreases to around 27 kJ mol^{-1} at 3.5 mmol g^{-1} adsorbed CO_2. The resulting heat of adsorption curve is somewhat different from the MOF-801 heat of adsorption reported in (Saidi et al., 2021), which descended from 30 to 25 kJ mol^{-1} over the same loading range. The isosteric heat of adsorption of N_2 was not calculated for the MOF-801 samples, as these isotherms did not fit the required isotherm models.

The Zeolite-13X-05 sample releases a lot of energy during the first 2.6 mmol g^{-1} of CO_2 adsorbed, before flattening out to a shallow curve stabilizing at around 30 kJ mol^{-1}, as shown in figure 5.20 to the right. The CO_2 heat of adsorption reported in (Streb & Mazzotti, 2021) for zeolite-13X stabilizes around 37-34 kJ mol^{-1}, and was calculated from isotherms measured at 298K, 318K and 338K. The isosteric heat of adsorption reported in this paper is somewhat higher than the result of Zeolite-13X-05. The high heat of adsorption on the zeolite for CO_2 is caused by the steep increase in quantity adsorbed at the lower pressures range. N_2 isosteric heat of adsorption has a constant value of 43.4 kJ mol^{-1}, as a result of the Zeolite-13X-05 N_2 isotherms both being linear in the region measured. The CO_2 adsorption isotherm data for the Zeolite-13X-05 was fitted to a dual-site Langmuir model, and the N_2 data with Henry's law. Due to insufficient datapoints received at the lower pressure ranges during sorption analysis, the CO_2 heat of adsorption graph shown in figure 5.20 starts at around 2.4 mmol g-1.

The isosteric heat of adsorption calculated have a relatively high grade of uncertainty both shape wise and quantity of heat released, as the graphs are calculated by isotherms at only two different temperatures. More accurate isosteric heat of adsorption curves could be obtained by measuring isotherms at additional temperatures.

5.9 Post sorption PXRD analysis

The samples were analyzed using PXRD after the sorption analysis of the samples were complete to inspect if the MOF structure and crystallinity had endured the degassing and sorption. The samples prepared for the post analysis PXRD were suspended in ethanol to produce a slurry before being applied to the analysis chip. As a result of the small quantity of each sample left after the sorption analysis, the procedure was changed from post-synthesis PXRD. This method could result in a degree of uncertainty in the PXRD results when comparing it to pre-degas data. The post-sorption analysis data for the washed samples were not considered.

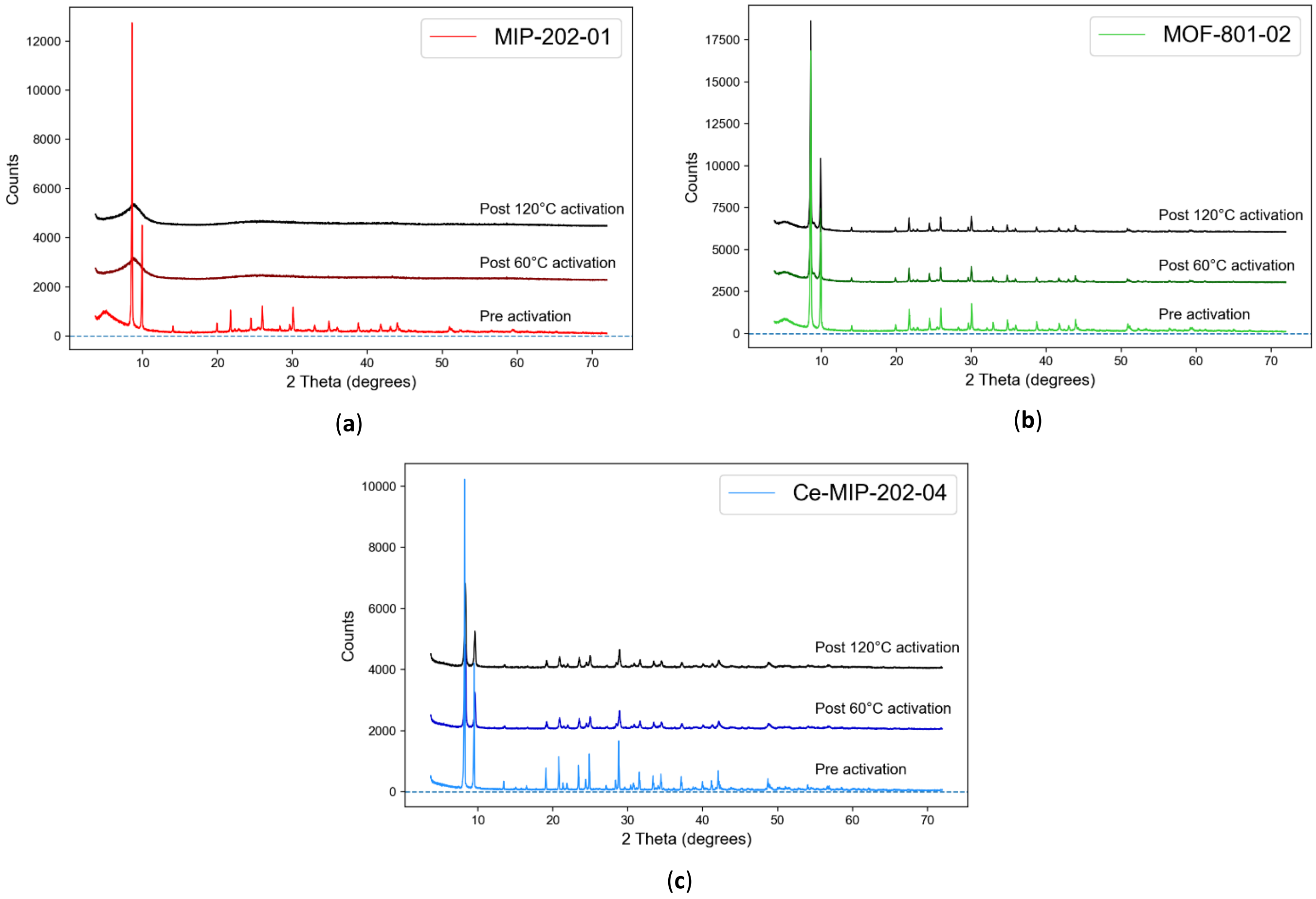

(a)

(b)

(c)

Figure 5.21. PXRD of (a) MIP-202-01, (b) MOF-801-02, (c) Ce-MIP-202-04, before and after degassing at 60°C and 120°C.

The MIP-202-01 structure, which before degassing gave a satisfactory PXRD graph, seemed to have collapsed, both after degassing at 60°C and 120°C. The collapse of the structure could explain the low CO2 and N2 uptake of the MIP-202-01. The MOF-801-02 appears to have remained intact after both 60°C and 120°C degassing, with a lesser decrease in intensity. The cerium-based Ce-MIP-202-04 sample had minor damages to the structure after both 60°C and 120°C, meaning the MOF still maintained its structure.

6 Conclusion and future work

6.1 Conclusion

The 77K N2 sorption data of the MIP-202 and the cerium-based MIP-202 samples were deviating so far from expected values and shapes that the samples were concluded to either be structurally impaired or with a completely different structure, which would be strange considering a low activation temperature and flawless PXRD results. The MIP-202-01 sample was also sensitive to the washing procedure, which also damaged the MOF significantly as seen in the PXRD of MIP-202-06. The main difference between the synthetic instructions and the performed synthesis was the choice of linkers, where the racemic mixture DL-Aspartic acid was used instead of the pure L-Aspartic acid isomer. The reaction time was also different, with 24 hours used for the sample in this thesis vs 72 hours in the original procedure. In (Skjærseth, 2021) there were reported significant differences between MIP-202 synthesized with D-aspartic acid and DL-aspartic acid, which further increases the possibility that isomer choice has an impact on MIP-202 properties.

In contrast to the MIP-202 samples which collapsed during degassing, the cerium-based MIP-202 samples seemed mostly to remain intact after degassing, only with minor structural damages. The N_2 sorption analysis, however, did not give satisfactory results in any of the cerium-based MIP-202 samples. The cerium-based MOFs were therefore concluded to be unusable for any carbon capture applications. There was also no improvement made on the different MOFs after washing treatments, rather a significant decrease. The direct cause is unknown, however some of the more likely causes could be due to degradation of the crystal structure or blocking of the pores by the molecules used in the washing steps.

Altogether, the untreated MOF-801 and the Zeolite 13X gave the most favorable results for high uptakes of CO_2 and low N_2. To conclude which would be of greatest benefit to apply to industry, a thorough techno-economic assessment with TSA and PSA experiments would have to be conducted on both. However, based on the operation isotherms of both materials alone, the Zeolite would come short when considering regeneration, as the temperature would have to become considerably high or with a near-vacuum pressure to flash the CO_2.

6.2 Future work

Some of the future work that can be done is to analyze MIP-202 with different isomers of aspartic acid to decide if specific isomer choice has a large effect on MIP-202 stability and properties, both with a D-isomer, L-isomer and with a racemic mixture. CO_2/N_2 adsorption isotherm data should be measured at additional temperatures besides 273K and 293K in future work to get more accurate isosteric heat of adsorption data. Sorption equipment with smaller incremental pressure steps at the lower pressure regions should also be used, as samples with high adsorptivity such as the zeolite 13X do not give sufficient datapoints on the lower quantities adsorbed, thus giving an incomplete isosteric heat of adsorption curve. The pore size distribution could also be characterized to gain more insight into the pore structure of the materials.

References

Boehle, T. (2010). *English: Large pore of MOF-5 with yellow ball*. Own work. https://commons.wikimedia.org/wiki/File:IRMOF-1_wiki.png

Broom, D. (2018, March 5). *Characterizing Adsorbents for Gas Separations*. https://www.aiche.org/resources/publications/cep/2018/march/characterizing-adsorbents-gas-separations

Chaudhary, A., & Prasad, E. (2021, August). *Carbon Capture, Utilization, and Storage Market Analysis—2030*. Allied Market Research. https://www.alliedmarketresearch.com/carbon-capture-and-utilization-market-A12116

Chen, W., Zhang, Z., Hou, L., Yang, C., Shen, H., Yang, K., & Wang, Z. (2020). Metal-organic framework MOF-801/PIM-1 mixed-matrix membranes for enhanced CO2/N2 separation performance. *Separation and Purification Technology*, *250*, 117198. https://doi.org/10.1016/j.seppur.2020.117198

Diab, K. E., Salama, E., Hassan, H. S., Abd El-moneim, A., & Elkady, M. F. (2021). Biocompatible MIP-202 Zr-MOF tunable sorbent for cost-effective decontamination of anionic and cationic pollutants from waste solutions. *Scientific Reports*, *11*(1), 6619. https://doi.org/10.1038/s41598-021-86140-2

Diab, K. E., Salama, E., Hassan, H. S., El-Moneim, A. A., & Elkady, M. F. (2021). Bio-Zirconium Metal-Organic Framework Regenerable Bio-Beads for the Effective Removal of Organophosphates from Polluted Water. *Polymers*, *13*(22), 3869. PubMed. https://doi.org/10.3390/polym13223869

Farha, O. K., & Hupp, J. T. (2010). Rational Design, Synthesis, Purification, and Activation of Metal−Organic Framework Materials. *Accounts of Chemical Research*, *43*(8), 1166–1175. https://doi.org/10.1021/ar1000617

Fraux, G., Boutin, A., Fuchs, A. H., & Coudert, F.-X. (2018). On the use of the IAST method for gas separation studies in porous materials with gate-opening behavior. *Adsorption*, *24*(3), 233–241. https://doi.org/10.1007/s10450-018-9942-5

Galarneau, A., Mehlhorn, D., Guenneau, F., Coasne, B., Villemot, F., Minoux, D., Aquino, C., & Dath, J.-P. (2018). Specific Surface Area Determination for Microporous/Mesoporous Materials: The Case of Mesoporous FAU-Y Zeolites. *Langmuir*, *34*(47), 14134–14142. https://doi.org/10.1021/acs.langmuir.8b02144

Geankoplis, C. J. (2003). *Transport processes and separation process principles: Includes unit operations* (4th ed). Prentice Hall Professional Technical Reference.

Giraldo, L., Rodriguez-Estupiñán, P., & Moreno-Piraján, J. C. (2019). Isosteric Heat: Comparative Study between Clausius–Clapeyron, CSK and Adsorption Calorimetry Methods. *Processes*, *7*(4). https://doi.org/10.3390/pr7040203

Guo, H., Liu, J., Li, Y., Caro, J., & Huang, A. (2021). Post-synthetic modification of highly stable UiO-66-NH2 membranes on porous ceramic tubes with enhanced H2 separation. *Microporous and Mesoporous Materials*, *313*, 110823. https://doi.org/10.1016/j.micromeso.2020.110823

Hönicke, I. M., Senkovska, I., Bon, V., Baburin, I. A., Bönisch, N., Raschke, S., Evans, J. D., & Kaskel, S. (2018). Balancing Mechanical Stability and Ultrahigh Porosity in Crystalline Framework Materials. *Angewandte Chemie International Edition*, *57*(42), 13780–13783. https://doi.org/10.1002/anie.201808240

Horikawa, T., Do, D. D., & Nicholson, D. (2011). Capillary condensation of adsorbates in porous materials. *Advances in Colloid and Interface Science*, *169*, 40–58. https://doi.org/10.1016/j.cis.2011.08.003

Hosa, A., Esentia, M., Stewart, J., & Haszeldine, S. (2010). *Benchmarking worldwide CO2 saline aquifer injections*. 70.

Jacobsen, J., Achenbach, B., Reinsch, H., Smolders, S., Lange, F.-D., Friedrichs, G., De Vos, D., & Stock, N. (2019). The first water-based synthesis of Ce(iv)-MOFs with saturated chiral and achiral C4-dicarboxylate linkers. *Dalton Transactions*, *48*(23), 8433–8441. https://doi.org/10.1039/C9DT01542F

Jahan, I., Rupam, T. H., Palash, M., Rocky, K. A., & Saha, B. B. (2022). Energy efficient green synthesized MOF-801 for adsorption cooling applications. *Journal of Molecular Liquids*, *345*, 117760. https://doi.org/10.1016/j.molliq.2021.117760

Ke, F., Peng, C., Zhang, T., Zhang, M., Zhou, C., Cai, H., Zhu, J., & Wan, X. (2018). Fumarate-based metal-organic frameworks as a new platform for highly selective removal of fluoride from brick tea. *Scientific Reports*, *8*. https://doi.org/10.1038/s41598-018-19277-2

Kumar, V., Srinivas, G., Wood, B., Ramisetty, K., Stewart, A., Howard, C., Brett, D. J. L., & Rodriguez-Reinoso, F. (2019). Characterization of adsorption site energies and heterogeneous surfaces of porous materials. *Journal of Materials Chemistry A*, *7*. https://doi.org/10.1039/C9TA00287A

Li, Y., Tang, Z., & Chen, C. (2021). The Modulating Effect of Ethanol on the Morphology of a Zr-Based Metal–Organic Framework at Room Temperature in a Cosolvent System. *Crystals*, *11*(4). https://doi.org/10.3390/cryst11040434

Lin, Y., Kong, C., & Chen, L. (2016). Amine-functionalized metal–organic frameworks: Structure, synthesis and applications. *RSC Advances*, *6*(39), 32598–32614. https://doi.org/10.1039/C6RA01536K

Majchrzak-Kucęba, I., & Ściubidło, A. (2019). Shaping metal–organic framework (MOF) powder materials for CO2 capture applications—A thermogravimetric study. *Journal of Thermal Analysis and Calorimetry*, *138*(6), 4139–4144. https://doi.org/10.1007/s10973-019-08314-5

Masika, E., & Mokaya, R. (2013). Preparation of ultrahigh surface area porous carbons templated using zeolite 13X for enhanced hydrogen storage. *Progress in Natural Science: Materials International*, *23*, 308–316. https://doi.org/10.1016/j.pnsc.2013.04.007

Mfoumou, C., Mignard, S., & Belin, T. (2018). The preferential adsorption sites of H 2 O on adsorption sites of CO 2 at low temperature onto NaX and BaX zeolites. *Adsorption Science & Technology*, *36*, 026361741876249. https://doi.org/10.1177/0263617418762494

Patterson, B. D., Mo, F., Borgschulte, A., Hillestad, M., Joos, F., Kristiansen, T., Sunde, S., & van Bokhoven, J. A. (2019). Renewable CO2 recycling and synthetic fuel production in a marine environment. *Proceedings of the National Academy of Sciences*, *116*(25), 12212–12219. https://doi.org/10.1073/pnas.1902335116

Saidi, M., Ho, P. H., Yadav, P., Salles, F., Charnay, C., Girard, L., Boukli-Hacene, L., & Trens, P. (2021). Zirconium-Based Metal Organic Frameworks for the Capture of Carbon Dioxide and Ethanol Vapour. A Comparative Study. *Molecules*, *26*(24), 7620. https://doi.org/10.3390/molecules26247620

Shokroo, E. J., Kakavandi, I. A., Baghbani, M., & Farniaei, M. (2017). Dynamic Modeling of Nitrogen Adsorption on Zeolite 13X Bed. *Fluid Mechanics Research International Journal*, *1*(1). https://doi.org/10.15406/fmrij.2017.01.00004

Simon, C. M., Smit, B., & Haranczyk, M. (2016). PyIAST: Ideal adsorbed solution theory (IAST) Python package. *Computer Physics Communications*, *200*, 364–380. https://doi.org/10.1016/j.cpc.2015.11.016

Skjærseth, P. (2021). *Synthesis optimization and characterization of MOFs for carbon capture*. 48.

Soni, S., Bajpai, P., & Arora, C. (2018). A review on metal-organic framework: Synthesis, properties and application. *Characterization and Application of Nanomaterials*, *2*. https://doi.org/10.24294/can.v2i2.551

Stanger, R., Wall, T., Spörl, R., Paneru, M., Grathwohl, S., Weidmann, M., Scheffknecht, G., McDonald, D., Myöhänen, K., Ritvanen, J., Rahiala, S., Hyppänen, T., Mletzko, J., Kather, A., & Santos, S. (2015). Oxyfuel combustion for CO2 capture in power plants. *International Journal of Greenhouse Gas Control*, *40*, 55–125. https://doi.org/10.1016/j.ijggc.2015.06.010

Streb, A., & Mazzotti, M. (2021). Adsorption for efficient low carbon hydrogen production: Part 1—Adsorption equilibrium and breakthrough studies for H2/CO2/CH4 on zeolite 13X. *Adsorption*, *27*(4), 541–558. https://doi.org/10.1007/s10450-021-00306-y

Sun, Y., Zheng, L., Yang, Y., Qian, X., Fu, T., Li, X., Yang, Z., Yan, H., Cui, C., & Tan, W. (2020). Metal–Organic Framework Nanocarriers for Drug Delivery in Biomedical Applications. *Nano-Micro Letters*, *12*(1), 103. https://doi.org/10.1007/s40820-020-00423-3

Thommes, M., Kaneko, K., Neimark, A. V., Olivier, J. P., Rodriguez-Reinoso, F., Rouquerol, J., & Sing, K. S. W. (2015). Physisorption of gases, with special reference to the evaluation of surface area and pore size distribution (IUPAC Technical Report). *Pure and Applied Chemistry*, *87*(9–10), 1051–1069. https://doi.org/10.1515/pac-2014-1117

Tun, H., & Chen, C.-C. (2021). Isosteric heat of adsorption from thermodynamic Langmuir isotherm. *Adsorption*, *27*(6), 979–989. https://doi.org/10.1007/s10450-020-00296-3

UNFCCC. (2020). *The Paris Agreement*. https://unfccc.int/process-and-meetings/the-paris-agreement/the-paris-agreement

Wang, S., Wahiduzzaman, M., Davis, L., Tissot, A., Shepard, W., Marrot, J., Martineau-Corcos, C., Hamdane, D., Maurin, G., Devautour-Vinot, S., & Serre, C. (2018). A robust zirconium amino acid metal-organic framework for proton conduction. *Nature Communications*, *9*(1), 4937. https://doi.org/10.1038/s41467-018-07414-4

Wei, M., Yu, Q., Duan, W., Limin, H., Liu, K., Qin, Q., Liu, S., & Dai, J. (2017). Equilibrium and Kinetics Analysis of CO 2 Adsorption on Waste Ion-exchange Resin-based Activated Carbon. *Journal of the Taiwan Institute of Chemical Engineers*, *77*. https://doi.org/10.1016/j.jtice.2017.04.040

Yu, C.-H., Huang, C.-H., & Tan, C.-S. (2012). A Review of CO 2 Capture by Absorption and Adsorption. *Aerosol and Air Quality Research*, *12*. https://doi.org/10.4209/aaqr.2012.05.0132

Appendix A

A.1

Python packages used and loaded in Jupyter Notebooks.

```
import numpy as np
import matplotlib.pyplot as plt
from sklearn.linear_model import LinearRegression
import pyiast
import pandas as pd
```

A.2

PXRD plot python script.

```
# Filenames
filename_1 = 'MOF-801-02'
filename_2 = 'MOF-801-02-60'
filename_3 = 'MOF-801-02-120'

# Dataframe loading
df1 = pd.read_csv(f'{filename_1}.xy', sep=' ', names=['x', 'y'])
df2 = pd.read_csv(f'{filename_2}.xy', sep=' ', names=['x', 'y'])
df3 = pd.read_csv(f'{filename_2}.xy', sep=' ', names=['x', 'y'])

# Plot parameters
plt.rcParams["font.family"] = "Arial"
plt.rcParams["figure.figsize"] = (8,5)

# y-axis correction of plots
df2['y'][20:] += 3000
df3['y'][20:] += 6000

plt.plot(df3['x'][20:], df3['y'][20:], linewidth=0.9, color='black')
plt.plot(df2['x'][20:], df2['y'][20:], linewidth=0.9, color='darkgreen')
plt.plot(df1['x'][20:], df1['y'][20:], linewidth=0.9, color='limegreen', label=filename_1)

# Graph description
plt.text(55, df1['y'].tail(1) + 700, 'Pre activation', fontsize=12)
plt.text(55, df2['y'].tail(1) + 700, 'Post 60°C activation', fontsize=12)
plt.text(55, df3['y'].tail(1) + 700, 'Post 120°C activation', fontsize=12)

plt.xlabel('2 Theta (degrees)', fontsize=13)
plt.ylabel('Counts', fontsize=13)
plt.legend(fontsize=18)
plt.axhline(1, linestyle='dashed', linewidth=1)

# Saving figure to file directory
plt.savefig(f'{filename_1} degass temperatures peak difference graph.png', dpi=200);
```

A.3

TGA plot python script.

```
def normalize_mass(df):
    endpoint = df['M'][df['M'].last_valid_index()]
    df['M'] = (df['M'] / endpoint) * 100

# Sample list
sample_dict = {1:['MIP-202-01', '$Zr_{6}$$O_{4}$$(OH)_{4}$$Asp_{6}$',
                  '$ZrO_{2}$', 'tab:red', 198.3],
               2:['MOF-801-02', '$Zr_{6}$$O_{4}$$(OH)_{4}$$Fum_{6}$',
                  '$ZrO_{2}$', 'tab:green', 184.5],
               3:['MOF-801-03', '$Zr_{6}$$O_{4}$$(OH)_{4}$$Fum_{6}$',
                  '$ZrO_{2}$', 'tab:pink', 184.5],
               4:['Ce-MIP-202-04', '$Ce_{6}$$O_{4}$$(OH)_{4}$$Asp_{6}$',
                  '$CeO_{2}$', 'tab:blue', 170.4],
               5:['Zeolite-13X-05', '', '', 'tab:orange', 0],
               6:['MIP-202-06', '$Zr_{6}$$O_{4}$$(OH)_{4}$$Asp_{6}$',
                  '$ZrO_{2}$', 'tab:cyan', 198.3],
               7:['Ce-MIP-202-07', '$Ce_{6}$$O_{4}$$(OH)_{4}$$Asp_{6}$',
                  '$CeO_{2}$', 'tab:olive', 170.4]}

####################################
# sample number

sample = 1

####################################

plt.rcParams["font.family"] = "Arial"
plt.rcParams["figure.figsize"] = (7,5)

# name of file
filename = sample_dict[sample][0]
# first product text
component_1 = sample_dict[sample][1]
# end product text
component_2 = sample_dict[sample][2]

df = pd.read_csv(f'{filename}.csv')
# Normalizing mass
normalize_mass(df)

plt.plot(df['T'], df['M'], color=sample_dict[sample][3], label='Mass')
plt.ylabel("Weight %", fontsize=13)
plt.xlabel("Temperature [$^\circ$C]", fontsize=13)
plt.ylim(bottom=50)
plt.title(filename, fontsize=14)

line_h_1 = sample_dict[sample][4]
line_h_2 = df['M'][df['M'].last_valid_index()]

# component text
plt.axhline(line_h_1,
            linestyle='dashed', linewidth=1)
plt.text(610, line_h_1 - 17, component_1, fontsize=12)
plt.axhline(line_h_2,
            linestyle='dashed', linewidth=1)
plt.text(610, line_h_2 - 17, component_2, fontsize=12)

if sample == 5:
    plt.ylim(top=120, bottom=80)
    plt.ylim(bottom=90)

# Saving figure to file directory
plt.savefig(f'{sample_dict[sample][0]} TGA graph.png', dpi=200);
```

A.4

Sample class and class creation python script.

```
class Sample:
    def __init__(self, filename, samplename, label):
        self.filename = filename
        self.samplename = samplename
        self.label = label
        self.sampletype = samplename.split()[0]
        self.temp = samplename.split()[-1]

        self.df = pd.read_csv(f"{self.filename}.csv")

        # Converting pressure from mmHg to kPa
        self.df['Pressure'] *= 0.133322
        # Converting cm^3/g to mmol/g
        self.df['Quantity'] /= 22.414

        self.dfP = self.df['Pressure']
        self.dfQ = self.df['Quantity']
```

A.5

BET transformation plot python script.

```python
# Functions:
def closest(lst, K):
    return lst[min(range(len(lst)), key = lambda i: abs(lst[i]-K))]

def y_val(p, V):
    return 1/(V*((1/p)-1))

#############################
# Sample:
sample = 'MOF-801-02-N2-77K'

#############################

# Finding closest values to 0.05 and 0.35 kPa:
ix_05 = np.where(samples[sample].dfP==closest(samples[sample].dfP, 0.05))[0][0]
ix_35 = np.where(samples[sample].dfP==closest(samples[sample].dfP, 0.35))[0][0]

bet_p = samples[sample].dfP[ix_05:ix_35].values.reshape(-1,1)
bet_q = samples[sample].dfQ[ix_05:ix_35].values.reshape(-1,1)
bet_y = y_val(bet_p, bet_q)

# adsorbed amount at 0.5 relative pressure:
ix_997 = np.where(samples[sample].dfP==closest(samples[sample].dfP, 0.5))[0][0]
load = samples[sample].dfQ[ix_997]
print(f'Loading at 0.5 relative pressure: {load:.2f}')

# Creating a linear regression model
model = LinearRegression().fit(bet_p, bet_y)
intercept = float(model.intercept_[0])
slope = float(model.coef_[0][0])
mlpv = 1/(slope + intercept)

# Printing regression parameters
print(f'r2: {model.score(bet_p, bet_y)}')
print(f'Slope: {slope}')
print(f'Intercept: {intercept}')
print()
print(f'Monolayer pore volume: {mlpv:.2f}')
print(f'BET surface area: {4.36 * mlpv:.2f}')
print(f'Total pore volume: {load/ 694:.4f}')

# Plotting regression line and extracted data points:
x_val = np.linspace(bet_p[0], bet_p[-1], 100)
plt.plot(x_val, x_val * slope + intercept,'--' , color=samples[sample].color)
plt.scatter(bet_p, bet_y, marker='p', color=samples[sample].color)
plt.xlabel('P/$P^o$', fontsize=13)
plt.ylabel('1/V($P^o$/P-1)', fontsize=12)
plt.title(f'BET plot - {samples[sample].sampletype}', fontsize=13)

# Plot axis limits
x_factor = (bet_p[-1] - bet_p[0]) * 0.2
y_factor = (bet_y[-1] - bet_y[0]) * 0.2
plt.xlim((bet_p[0] - x_factor,  bet_p[-1] + x_factor))
plt.ylim((bet_y[0] - y_factor,  bet_y[-1] + y_factor))

plt.grid();

# Saving figure to file directory
plt.savefig(f'{samples[sample].sampletype} BET Plot' , dpi=200)
```

A.6

A.6.1
Isotherm plot python script

```python
#############################
# Samples:

samplelist = ["Zeolite-13X-05-CO2-273K",
              "Zeolite-13X-05-N2-273K",
              "Zeolite-13X-05-CO2-293K",
              "Zeolite-13X-05-N2-293K"]

#############################

for i in samplelist:
    plt.plot(samples[i].dfP, samples[i].dfQ, label=samples[i].label)
    plt.scatter(samples[i].dfP, samples[i].dfQ, marker='.')

plt.xlabel(f'Absolute pressure [kPa]', fontsize=13)
plt.ylabel(f'Quantity adsorbed [mmol/g]', fontsize=13)
plt.legend()
plt.grid()
plt.title(samples[samplelist[0]].sampletype, fontsize=13);

# Saving figure to file directory
plt.savefig(f'{samples[samplelist[0]].sampletype} Isotherms', dpi=200)
```

A.6.2

IAST selectivity calculation and plot python script.

```
##########################################
# Samples:
samplelist = ["Zeolite-13X-05-CO2-293K",
              "Zeolite-13X-05-N2-293K",
              "Zeolite-13X-05-CO2-273K",
              "Zeolite-13X-05-N2-273K", ]

# CO2 fractions
CO2_fractions = [0.10, 0.50]
colors = ['blue', 'magenta']
pressure = 100

# Isotherm data models
CO2_model = 'DSLangmuir'
N2_model = 'Henry'
##########################################

# Fitted isotherms
isolist = list()
for i, sample in enumerate(samplelist):
    isolist.append(pyiast.ModelIsotherm(samples[sample].df,
                                        loading_key="Quantity", pressure_key="Pressure",
                                        model = N2_model if (i + 1) % 2 == 0 else CO2_model))
# Pressure range
pressures = np.linspace(min(samples[samplelist[0]].dfP), pressure, 1000)

for i, frac in enumerate(CO2_fractions):
    for j in [0, 2]:
        s_list = list()

        for p in pressures:

            partial_p = [p * frac, p * (1 - frac)]

            comp_load = pyiast.iast(partial_p, [isolist[j], isolist[j + 1]],
                                    verboseflag=False, warningoff=True)


            selectivity = (comp_load[0] / partial_p[0]) * (partial_p[1] / comp_load[1])
            s_list.append(selectivity)

        plt.plot(pressures, s_list, '--' if j > 1 else '-',
                 label=f'{samples[samplelist[j]].temp} $CO_{2}$ fraction: {str(frac)}', color=colors[i])

plt.ylabel('Selectivity', fontsize=13)
plt.xlabel(f'Absolute pressure [{pressure_unit}]', fontsize=13)
plt.title(f'$CO_{2}$/$N_{2}$ selectivity of {samples[samplelist[0]].sampletype}', fontsize=13)
plt.grid()
plt.legend(fontsize=12);

# Saving figure to file directory
plt.savefig(f'{samples[samplelist[0]].samplename} selectivity plot.png', dpi=200)
```

A.6.3

CO_2/N_2 gas coadsorption calculation and plot python script.

```
def plt_CO2_iso(sample):
    plt.plot(sample.dfP, sample.dfQ, label=f'CO2 isotherm', color='skyblue')
    plt.scatter(sample.dfP, sample.dfQ, marker='.', color='skyblue')

def plot_N2_iso(sample):
    plt.plot(sample.dfP, sample.dfQ, label=f'N2 isotherm', color='lightcoral')
    plt.scatter(sample.dfP, sample.dfQ, marker='.', color='lightcoral')

#############################
# Samples:
samplelist = ["Zeolite-13X-05-CO2-293K",
              "Zeolite-13X-05-N2-293K"]

frac_CO2 = 0.10
pressure = 100

#############################

pressures = np.linspace(min(samples[samplelist[0]].dfP), pressure, 1000)

CO2_iso = pyiast.ModelIsotherm(samples[samplelist[0]].df, loading_key="Quantity",
                               pressure_key="Pressure", model='DSLangmuir')
N2_iso = pyiast.ModelIsotherm(samples[samplelist[1]].df, loading_key="Quantity",
                              pressure_key="Pressure", model='Henry')

load_CO2_list = list()
load_N2_list = list()

for p in pressures:

    partial_p = [p * frac_CO2, p * (1 - frac_CO2)]

    comp_load = pyiast.iast(partial_p, [CO2_iso, N2_iso],
                            verboseflag=False, warningoff=True)

    load_CO2_list.append(comp_load[0])
    load_N2_list.append(comp_load[1])

plt.plot(pressures, load_CO2_list, label=f'CO2 IAST', color='royalblue')
plt_CO2_iso(samples[samplelist[0]])
plt.plot(pressures, load_N2_list, label=f'N2 IAST', color='firebrick')
plot_N2_iso(samples[samplelist[1]])

# fraction text
plt.text(max(pressures) - (max(pressures)/3), 1.2,
         f'$CO_{2}$ fraction: {frac_CO2:.3f}', fontsize=13)

plt.ylabel('Quantity adsorbed [mmol/g]', fontsize=13)
plt.xlabel(f'Pressure [{pressure_unit}]', fontsize=13)
plt.xlim((0, max(pressures)))
plt.title(f'{samples[samplelist[0]].samplename} coadsorption')
plt.grid()
plt.legend();

# Saving figure to file directory
plt.savefig(f'{samples[samplelist[0]].samplename} {plot_type} coadsorption comparison plot.png', dpi=200)
```

A.6.4

Direct selectivity calculation python script.

```
##########################################
# Samples:
samplelist = ["Zeolite-13X-05-CO2-293K",
              "Zeolite-13X-05-N2-293K",
              "Zeolite-13X-05-CO2-273K",
              "Zeolite-13X-05-N2-273K"]

CO2_fractions = [0.10, 0.50]
colors = ['blue', 'magenta']

##########################################

plt.rcParams["font.family"] = "Arial"
plt.rcParams["figure.figsize"] = (7,4)

for i, frac in enumerate(CO2_fractions):
    for j in [0, 2]:
        s_list = list()

        for p in range(len(samples[samplelist[j]].dfP)):
            # CO2 values
            xa = samples[samplelist[j]].dfQ[p]
            pa = samples[samplelist[j]].dfP[p] * frac
            # N2 values
            xb = samples[samplelist[j + 1]].dfQ[p]
            pb = samples[samplelist[j + 1]].dfP[p] * (1 - frac)


            selectivity = (xa / pa) * (pb / xb)
            s_list.append(selectivity)

        plt.plot(samples[samplelist[j]].dfP, s_list, '--' if j > 1 else '-',
                 label=f'{samples[samplelist[j]].temp} $CO_{2}$ fraction: {str(frac)}', color=colors[i])

plt.ylabel('Selectivity', fontsize=13)
plt.xlabel(f'Absolute pressure [kPa]', fontsize=13)
plt.title(f'$CO_{2}$/$N_{2}$ selectivity of {samples[samplelist[0]].sampletype}', fontsize=13)
plt.grid()
plt.legend(fontsize=12);

# Saving figure to file directory
plt.savefig(f'{samples[samplelist[0]].samplename} manual selectivity plot.png', dpi=200)
```

A.7

A.7.1

Isosteric heat of adsorption calculation functions python script.

```python
# Functions:
def closest(lst, K):
    return lst[min(range(len(lst)), key = lambda i: abs(lst[i]-K))]

# Isosteric heat of adsorption formula
def heat(p1, p2):
    return R * T1 * T2 / ((T2 - T1) * np.log(p1/p2))

# Henry's constant isotherm function
def henry(p_list, KH):
    return p_list * KH

# Langmuir isotherm function
def langmuir(p_list, M, K):
    return M * (K * p_list) / (1 + K * p_list)

# Dual-site Langmuir isotherm function
def dslangmuir(p_list, M1, M2, K1, K2):
    return M1 * K1 * p_list / (1 + K1 * p_list) + M2 * K2 * p_list / (1 + K2 * p_list)

# Modeling of isotherms and pressure values of each isotherm per loading value
def p_lists(sample, start_quantity, model):
    sample_293, sample_273 = f"{sample}-293K", f"{sample}-273K"
    p_list = np.linspace(1, 200, 10000)

    iso_293 = pyiast.ModelIsotherm(samples[sample_293].df, loading_key="Quantity",
                                        pressure_key="Pressure", model=model)
    iso_273 = pyiast.ModelIsotherm(samples[sample_273].df, loading_key="Quantity",
                                        pressure_key="Pressure", model=model)
    if model == 'Henry':
        load_293 = henry(p_list, iso_293.params['KH'])
        load_273 = henry(p_list, iso_273.params['KH'])

    if model == 'Langmuir':
        load_293 = langmuir(p_list, iso_293.params['M'], iso_293.params['K'])
        load_273 = langmuir(p_list, iso_273.params['M'], iso_273.params['K'])

    if model == 'DSLangmuir':
        load_293 = dslangmuir(p_list, iso_293.params['M1'], iso_293.params['M2'],
                              iso_293.params['K1'], iso_293.params['K2'])
        load_273 = dslangmuir(p_list, iso_273.params['M1'], iso_273.params['M2'],
                              iso_273.params['K1'], iso_273.params['K2'])

    loadings = np.linspace(start_quantity, max(load_293), 500)

    pl_293, pl_273 = list(), list()

    for load in loadings:
        pl_293.append(p_list[np.where(load_293==closest(load_293, load))])
        pl_273.append(p_list[np.where(load_273==closest(load_273, load))])

    return pl_293, pl_273, loadings
```

A.7.2

Isosteric heat of adsorption plot python script.

```python
#######################################################
# Sample
samplelist = ["Zeolite-13X-05-N2", "Zeolite-13X-05-CO2"]
# Temperature and gas constant parameters:
T1, T2, R = 293, 273, 8.314e-3

gaslist, color = ['$N_{2}$', '$CO_{2}$'], ['tab:red', 'tab:orange']
model, start = ['Henry', 'DSLangmuir'], [0.01, 2.7]

#######################################################

for j, samplename in enumerate(samplelist):
    heat_l = list()
    presl_293, presl_273, loadings = p_lists(samplename, start[j], model[j])

    for i in range(len(loadings)):
        heat_l.append(heat(presl_273[i], presl_293[i]))

    plt.plot(loadings, heat_l, color=color[j], label=gaslist[j])

plt.xlabel(f'quantity adsorbed [mmol/g]', fontsize=13)
plt.ylabel('Heat of adsorption [kJ/mol]', fontsize=13)
plt.title(f'Isosteric heat of adsorption for {samplename[:-4]}', fontsize=13)
# y-axis limits
plt.ylim((0, 60))
plt.legend(fontsize=13)
plt.grid();

# Saving figure to file directory
plt.savefig(f'{samplename} Heat of adsorption', dpi=200)
```

Appendix B

Table of EDS results for MIP-202-01 (B.1), MOF-801-02 (B.2), MOF-801-03 (B.3), Ce-MIP-202-04 (B.4), and Zeolite-13X-05 (B.5).

B.1

Element	Weight %	Atomic	Net Int.	Error %	Kratio	Z	A	F
N K	6.97	14.23	25.27	14.51	0.0121	1.2113	0.1431	1.0000
O K	32.51	58.04	246.66	9.84	0.0781	1.1861	0.2026	1.0000
Zr L	42.69	13.37	546.29	2.32	0.3633	0.8139	1.0435	1.0020
Cl K	17.83	14.36	298.51	4.52	0.1363	1.0043	0.7602	1.0012

B.2

Element	Weight %	Atomic	Net Int.	Error %	Kratio	Z	A	F
C K	39.46	59.32	134.43	11.56	0.0965	1.1208	0.2183	1.0000
O K	29.00	32.72	181.15	10.92	0.0659	1.0700	0.2125	1.0000
Zr L	26.03	5.15	267.41	4.36	0.2054	0.7304	1.0792	1.0010
Cl K	5.51	2.81	80.13	10.85	0.0424	0.9005	0.8527	1.0022

B.3

Element	Weight %	Atomic	Net Int.	Error %	Kratio	Z	A	F
C K	18.51	36.67	83.41	13.34	0.0362	1.2029	0.1624	1.0000
O K	32.51	48.36	376.81	10.26	0.0835	1.1506	0.2233	1.0000
Zr L	43.63	11.38	768.60	2.62	0.3613	0.7892	1.0485	1.0006
Cl K	5.35	3.59	123.51	8.47	0.0402	0.9737	0.7701	1.0015

B.4

Element	Weight %	Atomic	Net Int.	Error %	Kratio	Z	A	F
C K	13.13	27.06	142.79	7.92	0.0877	1.2459	0.5362	1.0000
N K	8.65	15.29	77.43	11.31	0.0363	1.2177	0.3445	1.0000
O K	31.97	49.48	477.35	8.30	0.1484	1.1928	0.3892	1.0000
Ce L	46.26	8.17	176.52	7.97	0.3493	0.7216	1.0461	1.0002

B.5

Element	Weight %	Atomic	Net Int.	Error %	Kratio	Z	A	F
O K	40.60	52.86	1046.64	6.63	0.2253	1.0650	0.5211	1.0000
Na K	14.97	13.57	402.13	6.11	0.0919	0.9623	0.6358	1.0030
Al K	20.48	15.81	754.64	4.38	0.1503	0.9398	0.7766	1.0054
Si K	23.94	17.76	816.54	4.71	0.1706	0.9592	0.7424	1.0007